Fluvial Features on Titan and Earth: Lessons from Planform Images in Low-resolution SAR

J. W. Miller[1,2], S. P. D. Birch[1,3] , A. G. Hayes[1], M. J. Malaska[4] , R. M. C. Lopes[4] , A. M. Schoenfeld[2,4], P. M. Corlies[3] ,
D. M. Burr[5], T. G. Farr[4], and JT Perron[3]

[1] Department of Astronomy, Cornell University, Ithaca, NY 14853, USA
[2] Department of Earth, Planetary, and Space Sciences, University of California, Los Angeles, Los Angeles, CA 90095, USA
[3] Department of Earth, Atmospheric, and Planetary Sciences, Massachusetts Institute of Technology, Cambridge, MA 02139, USA
[4] Jet Propulsion Laboratory, California Institute of Technology, Pasadena, CA 91109, USA
[5] Department of Astronomy and Planetary Sciences, Northern Arizona University, Flagstaff, AZ 86001, USA

Abstract

Cassini Synthetic Aperture Radar (SAR) images of Titan's surface revealed river networks strikingly similar to those on Earth. However, Cassini SAR has low spatial resolution and image quality compared to data used to map channels on Earth, so traditional methods for characterizing river networks might not yield accurate results on Titan. We mapped terrestrial analog networks with varying resolutions and image qualities to determine which geomorphologic metrics were invariant with scale or resolution. We found that branching angle and drainage density varied significantly with image resolution, and we therefore expect the actual drainage density of Titan's channel networks to be significantly higher than the values calculated from Cassini data. Calculated network geometry did not change predictably with resolution and would therefore not be an ideal metric for interpreting Titan's channel networks. The measured channel width, basin length and width, and drainage area all behaved predictably as resolution varied, leading us to conclude that these metrics could be applied to Cassini data. We then mapped all observable fluvial features on Titan—excluding those in the highly incised labyrinth terrains—visible in the Cassini data set. In our new maps, we observe differences in basin shapes between Titan's polar and equatorial regions and dichotomies in the relative channel density between the northern and southern midlatitudes and poles of Titan: channels are concentrated at the poles and southern midlatitudes. These patterns may reflect differences in bedrock material and/or different climate histories.

Unified Astronomy Thesaurus concepts: Titan (2186); Saturnian satellites (1427)

1. Introduction

While Earth's hydrologic systems are, by definition, water-based, the analog to water on Titan is liquid methane and ethane (Hayes 2016). Methane clouds in Titan's lower troposphere were first detected at low latitudes in ground-based observations (Griffith et al. 1998). The subsequent discovery and investigation of seasonal cloud coverage (Brown et al. 2002; Turtle et al. 2018) and observations of surface darkening (Turtle et al. 2011; Lopes et al. 2019) at the poles motivated predictions of methane rainfall and surface transport (Lora et al. 2015; Faulk et al. 2020).

Confirmation of atmosphere−surface interactions was provided by the Cassini RADAR instrument ($\lambda \sim 2.2$ cm) and the Huygens descent camera (visible wavelengths). Both data sets, though at far different spatial scales, show complex channel networks on the moon's surface. The channels are thought to have been carved into Titan's water ice and organic surface by flowing liquid methane (Tomasko et al. 2005; Perron et al. 2006; Soderblom et al. 2007; Lorenz et al. 2008; Burr et al. 2013a).

Channels are distinguished in Cassini Synthetic Aperture Radar (SAR) data as sinuous, radar backscatter contrasts that are either brighter or darker than the surrounding terrains (e.g., Tomasko et al. 2005; Lorenz et al. 2008; Burr et al. 2013a). Radar-dark

channels are interpreted by Poggiali et al. (2016) as being liquid filled or containing abundant fine-grained sediment. Radar altimetry data, obtained when the radar is pointing nadir, show specular reflections over a few of these radar-dark channels, confirming the presence of millimeter-scale smooth surfaces (possibly liquids) at the time of observation. As opposed to the radar-dark channels, the radar-bright channels are rough at the wavelength of the radar and/or contain material that is compositionally distinct from the surroundings. These features have been interpreted as braided streams or empty channel beds (Le Gall et al. 2010; Burr et al. 2013b), where the majority of the channel is filled with loose centimeter-sized (or greater) sediment.

Channels on Titan have also been observed to have a variety of morphologies, including dendritic (Perron et al. 2006) and rectilinear (Burr et al. 2013a) networks, possible canyons (Poggiali et al. 2016), and sinuous paths that may be meanders (Malaska et al. 2011). A selection of different channel morphologies is shown in Figure 1. The termini of many networks also feature possible sedimentary deposits, including alluvial fans (Birch et al. 2016; Radebaugh et al. 2018) and deltaic features near Ontario Lacus (Wall et al. 2010), suggesting that some channels have transported sediment in the recent past.

The spatial distribution of channels (Jaumann et al. 2008; Lorenz et al. 2008; Langhans et al. 2011; Black et al. 2017), the variability of their morphology with latitude or geomorphic region (Lorenz et al. 2008; Lunine & Atreya 2008; Burr et al. 2009; Lopes et al. 2010; Langhans et al. 2011; Black et al. 2012; Tewelde et al. 2013), and their spectral characteristics (Langhans et al. 2011) have all been classified to various degrees throughout
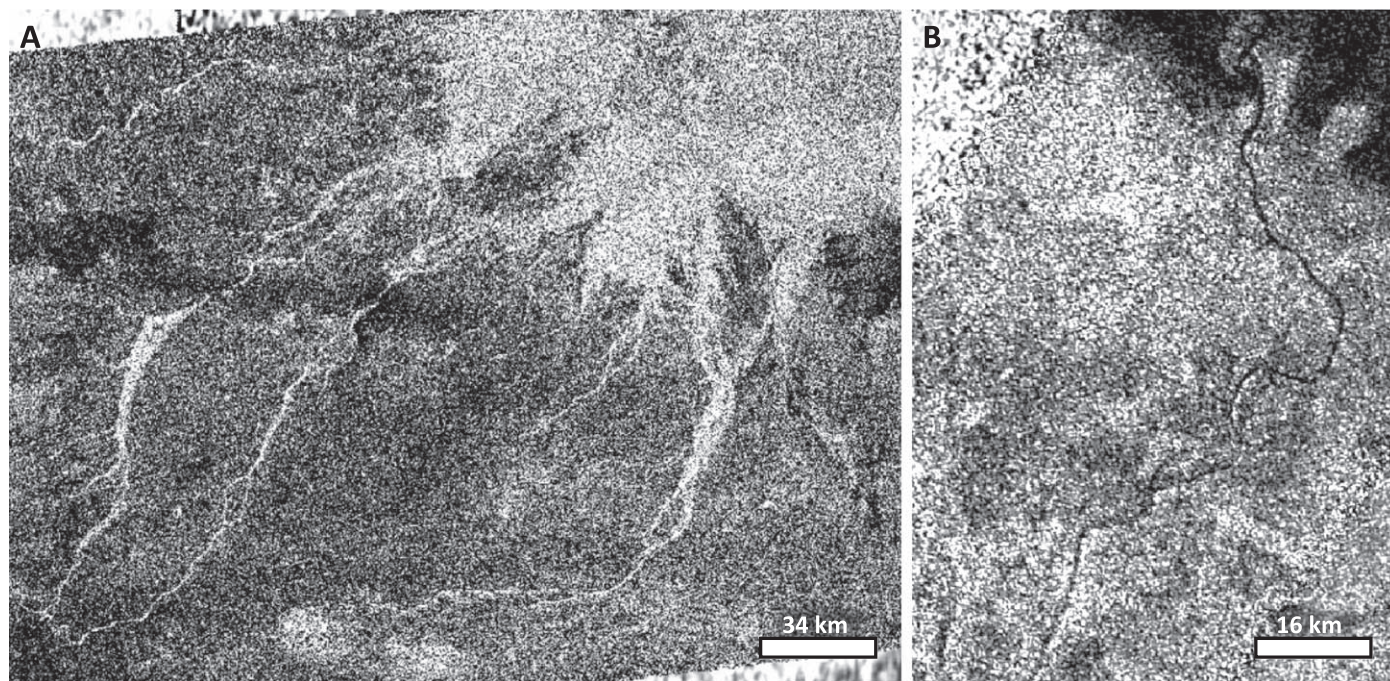
Figure 1. (A) Elvigar Flumina: a network of radar-bright channels near Menrva Crater in Titan's equatorial region. (B) Saraswati Flumina: a liquid-filled channel draining into Ontario Lacus, with two potential deltas at the river−sea margin (Wall et al. 2010).

the Cassini mission. However, due to Cassini's coarse resolution and limited coverage, we do not yet know whether there is systematic variation in morphologic type indicative of heterogeneities in the crust (e.g., tectonic control; Burr et al. 2013a) and/ or a variation in transport efficiencies or climate change (e.g., equatorial drying; Moore et al. 2014). These uncertainties necessitated a comprehensive map of Titan's channels based on all available data.

In Section 2, we leverage terrestrial channel networks as analogs to those on Titan. Analyzing them at various resolutions, and with or without added speckle noise, we gain new insight into the challenges inherent in analyzing relatively sparse, low-resolution radar images of fluvial networks. In Section 3, we determine which traditional, Earth-based geomorphologic metrics provide the most robust results when applied to Titan's channels and use these metrics to infer characteristics of the moon's surface.

In Section 4, we show an updated map of Titan's channels that utilizes the complete SAR data sets of the Cassini-Huygens mission. This new map provides coverage of about 60% of the moon at spatial resolutions of $1.7 \, \mathrm{km \, pixel^{-1}}$ or better, increased coverage at resolutions down to 350 m, and a greater degree of overlap between swaths (Wall et al. 2019). We have mapped all channels on Titan observable in the SAR data set, excluding potential near- or sub-resolution channels that may be present within labyrinth terrains, defined by Malaska et al. (2020) as "highly dissected organic plateaux."

This new map and analysis have the benefit of both more and higher-resolution surface coverage. However, our view of Titan remains significantly limited, in terms of both resolution and the extent of the coverage, compared to terrestrial data sets. We hypothesize that these limitations make some terrestrial metrics used to characterize fluvial features less robust.

2. Mapping Methodology

For our terrestrial mapping, channel selection at various resolutions was determined by a single individual. Two data sets were used to investigate channels on Earth: high-resolution visible images from SPOT 6/7 (visible wavelengths with spatial resolution of $2.5 \, \mathrm{m \, pixel^{-1}}$) and slightly lower-resolution SAR images from Sentinel-1 (5.5 cm wavelength with spatial resolution of $10–30 \, \mathrm{m \, pixel^{-1}}$; Torres et al. 2012). The terrestrial SAR images were ultimately downgraded to the spatial resolution of the artificially enhanced Cassini SAR, with multiplicative speckle noise added to approximate the noise characteristics present within the Cassini SAR data (Section 2.2). Visible channels were mapped from the Earth data at each resolution, and channels mapped at the lowest resolution were classified by degree of certainty that they corresponded to real features. Metrics were calculated for all mapped channels as described in Section 2.4. In order to avoid bias, the simulated low-resolution and noisy data were mapped first, followed by the higher-resolution data afterward (Figure 2).

In the terrestrial "Cassini-quality" ($350 \, \mathrm{m \, pixel^{-1}}$ with added speckle noise) images, there were not enough high-certainty channels mapped in any network to produce statistically significant results for metrics like network geometry and average branching angle. Burr et al. (2013a) determined that a minimum of 10 links were required to produce accurate classification results for a network. None of the networks mapped in this study met that criterion once low-certainty channels were removed.

Ideally, larger networks would be mapped to avoid this issue, but networks large enough to give significant results would have to be some of the largest on Earth (e.g., the Amazon). These largest networks tend to be highly vegetated and altered (dams, levees, etc.) by humans, bringing into question the influence such features would have on their rivers' detectability and their subsequent applicability to Titan. For
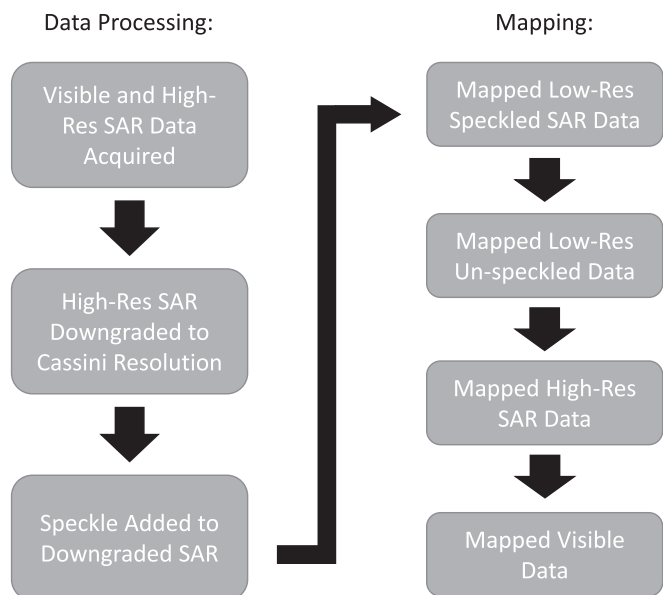
Data Processing:

Mapping:

Figure 2. Representation of our process for processing and mapping from terrestrial data.

example, vegetation artificially makes such channels easier to detect (Elachi & van Zyl 2006), concrete levees will show up as clear dielectric contrasts (Elachi & van Zyl 2006), and dams artificially increase the channel width upstream for some distance. All three effects increase the contrast such channels would have with their surroundings and would introduce a significant bias in our methodology that we would be unable to remove. Since the purpose of this study was to determine how changes in resolution and image quality affect channel visibility, data at $2\times$ Cassini resolution (175 m pixel^{-1} with added speckle noise: twice as good as Cassini's resolution) could still be used to produce meaningful results, and so we strove to map the most remote, well-imaged, and largest channels available. Accordingly, the lowest-quality down-graded data used in this study were 175 m pixel^{-1}, with the same process described above used to create "$2\times$ Cassini-quality" images.

For our Titan mapping, to add an additional level of completeness to our final product, we had two individuals map all of Titan's channels independently. The resulting maps of Titan were then tested against each other to ensure maximal consistency in mapping while minimizing bias in the final map of Titan's channels. After validating the map, we then combined them into a single map (Section 4.1). Channels on Titan were mapped from the complete set of Cassini SAR data.

2.1. Remote Sensing Data

2.1.1. Terrestrial Maps

The highest-resolution visible maps used were part of the Esri World Imagery map layer, available as a world imagery basemap in ArcMap. These optical images of Earth's surface were taken by SPOT 6/7 at 2.5 m pixel^{-1} or better.

Though radar is useful in mapping the presence/absence of fluid within channels owing to its ability to peer through clouds (e.g., Klemenjak et al. 2012; Buono et al. 2017), typically, terrestrial river networks and the landscapes pertinent to the evolution of drainage basins are not studied at radar wavelengths. This difference is likely due to the widespread availability of

high-resolution visible-wavelength images, which are preferable because they are more similar to what our eyes are used to seeing. To understand how well radar data represent fluvial systems, we utilized Sentinel-1 data to perform similar channel mapping at radar wavelengths. The Sentinel-1 C-SAR instrument operates at a wavelength of 5.5 cm (approximately twice that of Cassini SAR) and collects data at an incidence angle between $20°$ and $46°$ (Torres et al. 2012), with spatial resolution ranging from 10 to 30 m pixel^{-1} depending on the mode. Because the scattering properties of a surface are a strong function of the radar wavelength and incidence angle, we chose Sentinel-1 as a result of both the availability of data and the similarity in wavelength to Cassini SAR (5.5 and 2.2 cm, respectively). The Sentinel-1 instrument produces both linear (vertically) and cross-polarized data, the former of which were used here for their similarity to Cassini data.

Note that while incidence angles likely influence our ability to resolve features and are known to impact image quality and feature mapping on Titan, the Sentinel-1 data did not provide significant variations owing to the nature of how the data were collected. Cassini SAR is acquired at varying incidence angles owing to the flyby nature of the spacecraft, while Sentinel-1 is instead able to control its geometry. Thus, our terrestrial SAR data set is limited to a narrow range of incidence angles ($29°$–$46°$).

2.1.2. Titan Maps

All channel mapping performed on Titan utilized Cassini SAR mosaics that we developed using every individual SAR swath (up to and including T126) acquired by Cassini throughout its mission. This final Cassini SAR data set increased the surface coverage from 29% in 2013 (resolutions <1 km pixel^{-1}), at the time of the previously published mapping of Burr et al. (2013a), to 46% for our mapping here (again, for resolutions <1 km pixel^{-1}). Whereas most of the mapping was performed on our mosaic, in places of overlap between swaths, each swath was individually examined to ensure completeness. We then mapped channels from the swath with the highest image quality. Although the highest spatial resolution of the raw data was around 240 m pixel^{-1} with an average of 350 m pixel^{-1} in the center of most swaths, images were projected up to 175 m pixel^{-1} (256 pixels per degree) to ensure that no useful information was down-sampled. Note that this up-sampling is performed during the Cassini SAR processing stage and the data set is freely available to the community on the PDS.

Due to the unique geometry of each of Cassini's flybys of Titan, the spatial resolution varies between swaths and across individual swaths from hundreds to thousands of meters. As part of the mosaic we developed, we also created, and utilized, a map of Cassini spatial resolution in our mapping to assess channel certainty (Figure A1).

Cassini SAR data are linearly same-sense polarized. Polarization can reveal the structure, orientation, and environmental conditions of surface elements. Linearly oriented structures such as dunes or ripples tend to reflect and preserve the polarization, while randomly oriented structures depolarize the signal as it bounces multiple times. While dominantly horizontal, the relative proportions of vertical and horizontal components of the polarization vary from flyby to flyby. Our choice of the linearly polarized Sentinel-1 data provides the closest analog to how Cassini observed Titan.
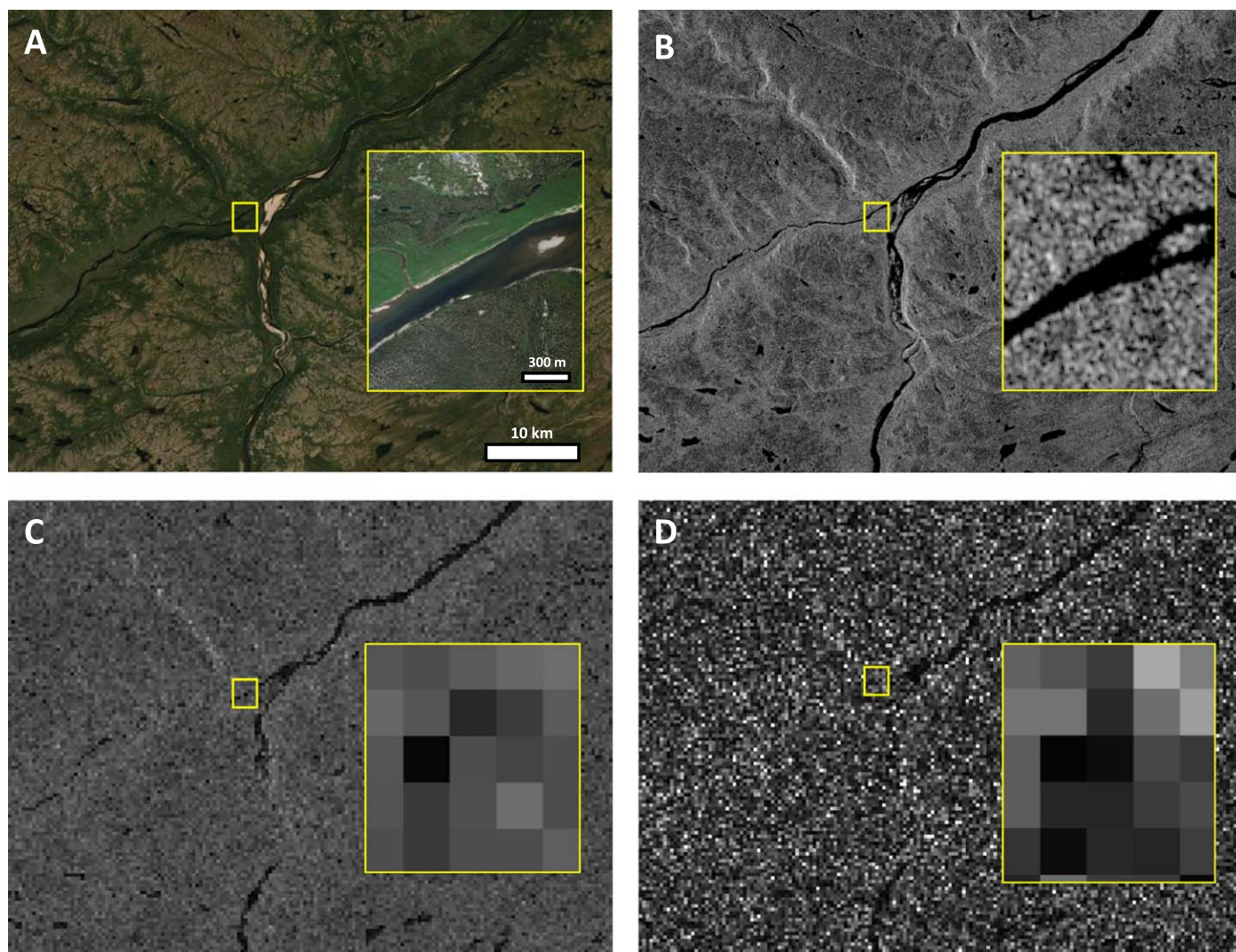
Figure 3. (A) SPOT visible image of an area in northern Quebec at the scale it was mapped (1:60,000). (B) Sentinel-1 SAR-C data in the same area with a spatial resolution of 30 m pixel^{-1}. (C) The same data downgraded to 350 m pixel^{-1} by calculating mean pixel values. (D) Downgraded data with added speckle noise.

Cassini SAR imaging was performed at incidence angles ranging from as low as 2° (almost directly overhead) to 69° (Wall et al. 2019), with an average incidence angle around 20°. The azimuth ("look") direction was fixed by the dynamics of a given flyby and was determined in our mapping by analyzing the corresponding incidence angle information (Figure A2). Both the incidence and azimuth angles allowed us to distinguish channels and depressions from ridges and rises (see Section 4.2).

2.2. Image Degradation

To simulate terrestrial data comparable to the highest-quality Cassini SAR images, Sentinel-1 SAR-C data at 10 m pixel^{-1} scales were first downgraded by averaging neighboring pixel values within 350 m × 350 m nonoverlapping windows. In addition to mapping on the visible-wavelength 2.5 m pixel^{-1} images and the SAR 10 m pixel^{-1} images, we also mapped all observable channels in this 350 m pixel^{-1} data set to understand the effects of pixel size on channel visibility.

Importantly, pixel size is not the only factor that impacts image resolution. Image noise is also convolved with the pixel size, and these factors together determine the image "resolution" (i.e., image quality, or what one can resolve in an image). For visible-wavelength imaging systems (hereafter termed "visible images"), the signal-to-noise ratio (S/N) is typically dominated by the Poisson statistics of photon arrival rates. For radar systems, the S/N is dominated by multiplicative speckle noise that arises from the coherent and incoherent interaction of scatters throughout a given resolution cell. Speckle noise is reduced by spatial or temporal averaging, reported as the number of "looks" used to generate each pixel in an SAR image. For Cassini, the number of looks typically ranged from 1 to 3, with the resulting speckle noise accounting for the "salt-and-pepper-like" appearance of most Cassini SAR images (Lucas et al. 2014). For more detailed information on this topic, see Elachi & van Zyl (2006) and Wall et al. (2019).

To model speckle noise and produce a map of similar resolution to the Titan data, we multiplied each 350 m image pixel by a random draw from an exponential noise distribution with a mean of 1 (Elachi & van Zyl 2006). To simulate multiple looks, this multiplication was done multiple times and the results were averaged together. As Cassini images typically have 1–3 looks, we used 3 looks as a representation of a best-case "Cassini-quality" image. The process is shown below in Figure 3.
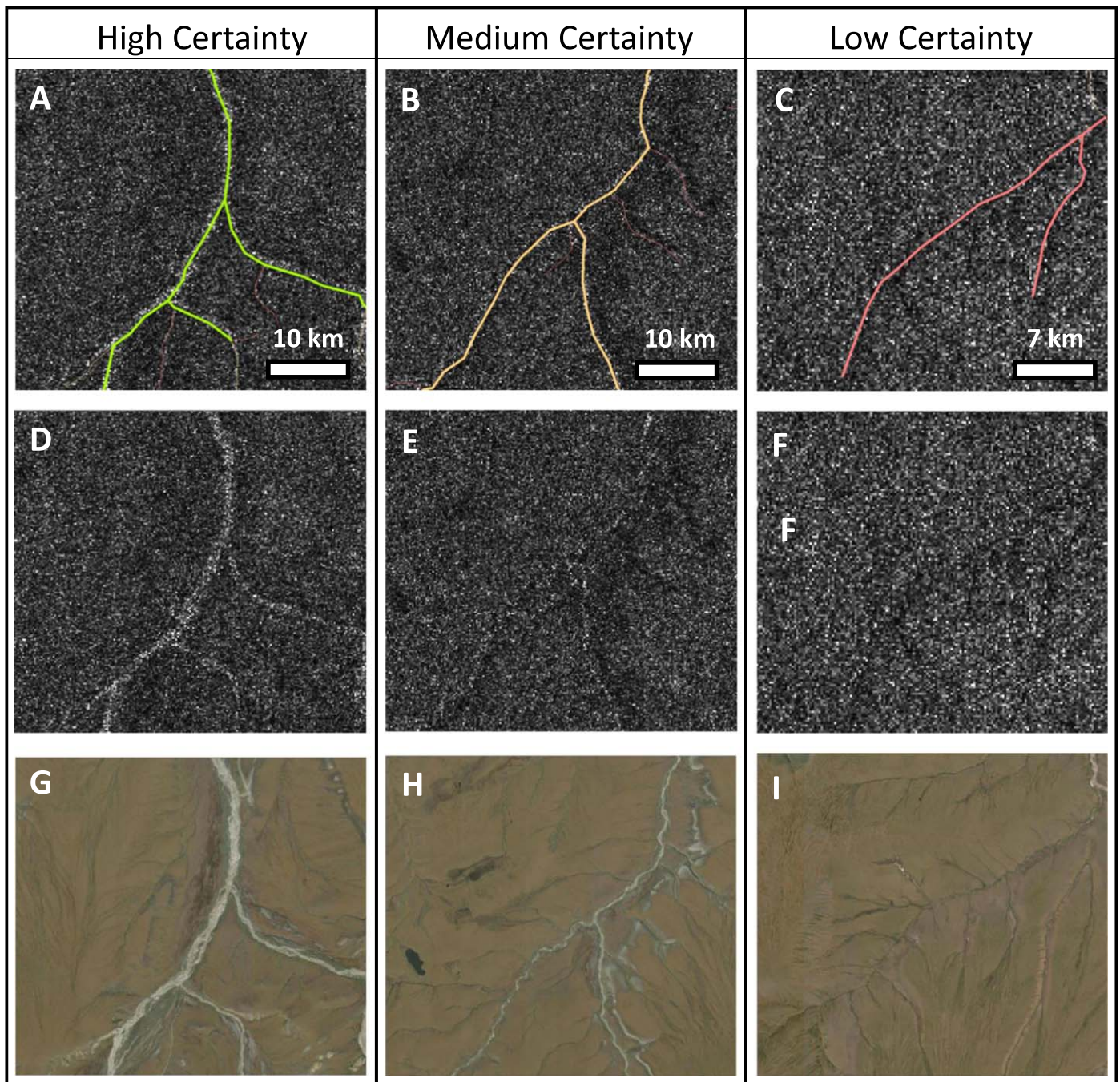
Figure 4. Images of channels mapped in Alaska. (A) Examples of high-certainty channels, which have clear edges and can be confidently traced along their entire path. (B) Medium-certainty channels, where parts of paths may be unclear. (C) Low-certainty channels, which may or may not be physical features. Images (A)–(F) show three different regions in downgraded Sentinel-1 SAR with mapping shown (A)–(C) and removed for clarity (D)–(F). Images (G), (H), and (I): corresponding regions in SPOT visible data.

This same process was also done to downgrade the original high-resolution SAR data to 175 m pixel^{-1}, since the 350 m pixel^{-1} "Cassini-quality" images could not be used to calculate some metrics (Section 2).

2.3. Mapping Certainty

Data were used from three locations on Earth (located in Alaska, northern Quebec, and western Australia; See Section 3.1 for more detail), with map segments about 400 km × 500 km. Each location on Earth was mapped four times. First, we mapped using the 2× Cassini-quality data, followed by the low-resolution

radar with no added speckle (175 m pixel^{-1} downgraded SAR) data. We then mapped a third time using the high-resolution radar (10–30 m pixel^{-1} Sentinel-1 SAR) data, and finally the visible images (using SPOT data).

All visible channels within a designated area were mapped by the same individual at each of the four scales. For our 2× Cassini-quality mapping effort, we colored channel segments corresponding to certainty (Figure 4). A high-certainty channel has clearly defined edges (which may correspond to channel banks, floodplain edges, or the width of the valley floor for different fluvial features) and can be traced confidently

along its entire path. A medium-certainty channel might contrast less clearly with its surroundings, and some portions of it may be unclear, but it appears unlikely to result from speckle noise alone. A low-certainty channel is a segment that appears linear but is not unambiguously a channel. This certainty metric was applied qualitatively to determine whether the lowest-certainty channel segments tended to correspond to channels in the higher-quality maps, or whether they tended to be the results of noise in the data.

To validate this qualitative metric, two networks were chosen within both the Australia and Alaska regions and were mapped three times, at all scales. This mapping was done by the same individual, but the same area was not mapped more than once per week, and other areas were mapped during that time period, to minimize bias from familiarity with a given region. This process allowed us to determine the consistency in our mapping and certainty classification and to constrain errors in branching angle measurements (Section 2.4). With the experience gained from our terrestrial mapping, we applied these same metrics during our mapping on Titan.

2.4. Measured Channel Metrics

Several metrics were chosen that could be measured or calculated for both Earth and Titan. On Earth, these metrics are used to relate properties of channels to broader factors such as hillslope processes and regional climate (Dietrich et al. 2003). To determine whether the same process could be done on Titan, we investigated how these metrics changed with resolution and image quality.

2.4.1. Width

Channel width is a key measurable of a fluvial network with a relation to stream discharge, accurate measurements of which will aid in estimating the erosional history of Titan's landscapes (Leopold & Maddock 1953; Chang 1980; Montgomery & Gran 2001).

On Earth, the width of a channel is determined using topographic data and/or on the ground by visual identification (Leopold & Maddock 1953). On Titan, we lack global high-resolution topographic data sets and have no in situ capabilities at present. Instead, we rely on measurements from planform image data. In the terrestrial visible image data, we observe a clear visual contrast in the image data between the high-albedo channel feature and the surrounding terrains (Figures 4(G)–(I)). We measured the channel width as the extent of the high-albedo material, which we assumed to represent the exposed portion of the channel present at low discharge. This assumption made comparisons with SAR images more straightforward, since the exposed portion of the bed on Titan also contrasts with its surroundings, appearing radar-bright and easily distinguishable (Figure 4). For liquid-filled channels on Earth, the width measurement was more straightforward, as we measured the width of the radar-dark feature, with no considerations of the current discharge.

We note that our measures of channel width are not direct determinations of an exact channel width. For the high-resolution and visible images, this is not as severe a problem, as it is possible to separate what appears to be the active channel from the surrounding terrains. For low-resolution, noisy planform images, however, it is difficult without other supporting data (e.g., topography) to precisely determine whether the measured width is that of the active channel bed (i.e., the bankfull discharge), or whether it included portions of the surrounding floodplains and valleys. The widths reported in this study accordingly represent maximum values.

Instead of measuring absolute values, we are interested in the differences in measured planform widths as resolution varies for the same images. Thus, we focus on consistently mapping the same feature in all images to determine whether image resolution affects our ability to measure a channel width. We therefore quote percent changes in the measured channel widths at different resolutions, for features we can reliably map on Earth. How our measures in the change of channel width with resolution transfers to Titan, where it is not known whether we are measuring floodplain widths of large braided rivers (for radar-bright channels) or flooded valleys (for radar-dark channels), remains to be determined. We note, however, that even estimates of maximum channel width may be useful for studies of Titan's geomorphology, such as hydraulic geometry calculations (e.g., Parker et al. 2007).

2.4.2. Minimum Drainage Area

River discharge is proportional to drainage area (see Dunne & Leopold 1979, and many subsequent works), and drainage area could therefore be used to investigate properties such as sediment transport, channel shape, and the composition of the liquid. This last concept is discussed by Lorenz (2014). Drainage area can also be used as an input to calculate metrics such as drainage density and basin aspect ratio that may provide information about hillslope processes in a region. Because minimum drainage area is used in these calculations, the calculated drainage density represents the maximum value for a given length of channels, and the calculated basin width/length represents minimum values.

Minimum drainage basins were mapped by connecting stream terminations with the method used for mapping basins in low-resolution images on Mars (Cabrol & Grin 2001) and recently for valley networks in labyrinth terrains on Titan (Malaska et al. 2020). It was done at each scale for all networks that were visible. Along with total link length, the minimum drainage area allowed us to assess the drainage density for each network at each resolution.

2.4.3. Drainage Density

On Earth, drainage density is affected by the magnitude and frequency of precipitation (Abrahams 1984), the hydraulic conductivity and nature of hillslopes, soil strength (Montgomery & Dietrich 1989), topographic relief (Horton 1945), and other factors, most of which are unknown on Titan.

Effective minimum drainage density was estimated by dividing the total length of channels in a given network by the minimum drainage area of that network. This process was done for all networks seen at all three scales. The total length of channels is assumed to be an underrepresentation at each scale, but this effect is more substantial in lower-resolution images in which only the largest channels are visible. Since both values used in the calculation for drainage density are likely lower bounds but not necessarily to the same extent, the resulting values for drainage density represent neither minima nor maxima.

2.4.4. Junction Angle

In addition to their use as a component in automated network classification, average branching angles have been shown to relate to climate. Though controlled by a complicated series of feedbacks, junction angles, and therefore basin widths, tended to be narrower in drier climates and wider in more humid regions (Seybold et al. 2017). Seybold et al. (2017) argue that this was driven by influence of groundwater flow on the ability to form and sustain channels, where drier climates had lower groundwater tables. However, considerable debate remains, especially for the largest channels, where a myriad of other dynamics are equally, or even more, important.

Branching angles were calculated for all intersections, and average branching angles of individual networks were computed for each map. The branching angle for each intersection of two channel links was calculated by fitting a straight line with a length of 5 pixels along each link, with the size of the pixel determined by the resolution of the data for the given data set. We specifically used the techniques described in Burr et al. (2013a) for determining the branching angles and network classification to allow direct comparisons with their results.

2.4.5. Basin Aspect Ratio

Techniques for the measurement of basin shape were adapted from a study by Yi et al. (2018). They found that the aspect ratio of basin width divided by basin length, on Earth, was related to a region's climate, with wider basins occurring more often in humid regions. Channel networks in humid regions were shown previously to have wider branching angles than networks in arid environments (Seybold et al. 2017), resulting in wider drainage basins (Yi et al. 2018).

Yi et al. (2018) defined basin width as drainage area divided by basin length, assuming that individual basins do not differ significantly in their overall planform shape (i.e., we consider relative differences between basins). Since basin length is difficult to determine without topographic data, the length of the longest channel path was used in this study instead.

A related metric is the width function described by Black et al. (2012)—the frequency distribution of along-network distances from the basin outlet—which should generally correlate with the width-to-length ratio of basins. This is likely to be among the more robust types of drainage network metrics but is more complicated to compute and is not used in this study.

2.4.6. Network Geometry

It has long been known that rock type and channel slope both have an effect on the morphology of river networks, and much work has been done to back out geologic information from aerial photographs of rivers on Earth. Parvis (1950) found that rectangular networks tend to be produced when streams follow faults and jointed rock, so that the predominance of rectangular networks in a region might indicate significant tectonic activity. He also wrote that a parallel drainage pattern is indicative of a "pronounced regional slope," while dendritic patterns are found where streams flow "in horizontal homogeneous rock." Howard (1967) later expanded on this idea, writing that "in any one small area where all other factors are constant, drainage texture may provide information on underlying materials and indirectly on structure." Reliable classification of Titan's networks could

therefore provide indirect information about Titan's bedrock material, topography, and tectonic activity.

The classification system used in this paper was laid out in Section 3.2 of Burr et al. (2013a) and originally adapted from Ichoku & Chorowicz (1994), who developed an automated river network classification scheme. Burr et al. (2013a) prescribe in their model only the broad categories of rectangular, parallel, and dendritic networks as options for classification, as the ability to make subtler distinctions between network types is constrained by the data available for channels on Titan. The resolution of Cassini SAR is insufficient, for instance, to reliably measure the "curvedness" of a channel within its banks.

A network was first tested for rectangularity using three separate conditions and was classified as rectangular if it met any one of the three conditions. Trunk channel links, used in one of these conditions, were defined here as links with Shreve stream order of at least 10. If the network did not meet any criteria for rectangularity, it was next tested for parallelism using three different conditions. If it met any one of these conditions, it was classified as parallel. If not, it was subjected to three more tests to determine whether the network was dendritic. If it passed all three tests, it was classified as dendritic. If it did not, the network was considered "unclassified." The specific conditions for each classification type are provided in detail in Burr et al. (2013a), and we refer the reader to their work for more information.

3. Terrestrial Results

3.1. Terrestrial Mapping Locations

Earth data were used in this study to understand the effect of remote sensing wavelength, image noise, and image pixel size on channel visibility and what that might imply for the low-resolution SAR images available of Titan's surface. It is difficult to determine which terrestrial rivers would be the best analogs for rivers on Titan (i.e., which of Titan's channels are alluvial versus detachment limited, if either), since channel beds are not directly visible in Cassini data and there are no high-resolution topographic data for channels on Titan. Lack of information about Titan's surface properties (such as near surface structure and porosity) prevents an understanding of how the surface scatters radio waves, so we assume here that it behaves similarly to the surface of Earth. Since Earth's rivers should be easier to discern owing to differences in material properties (i.e., water is far more absorptive than methane or ethane; Mitchell et al. 2015), we believe that this is a conservative assumption.

Given the limited data we have of Titan, we chose locations of Earth that were as similar as possible to the surface of Titan: river networks spanning hundreds of kilometers, with relatively mild topographic relief (<1 km), and a limited influence of humans and vegetation. Maps of channels were made for three regions that fit these criteria, shown in Figure 5. Note that in all our mapping, we are limited to the available data of the three regions—the SAR and visible data sets are not temporally coincident. We are therefore unable to account for seasonal variations in the mapping regions that may have occurred between the times when the data sets were acquired. We assume that such variations are minimal compared to variations due to wavelength, resolution, and/or noise.

The terrestrial networks used in this study are smaller than many of those observed on Titan. It is very difficult to find
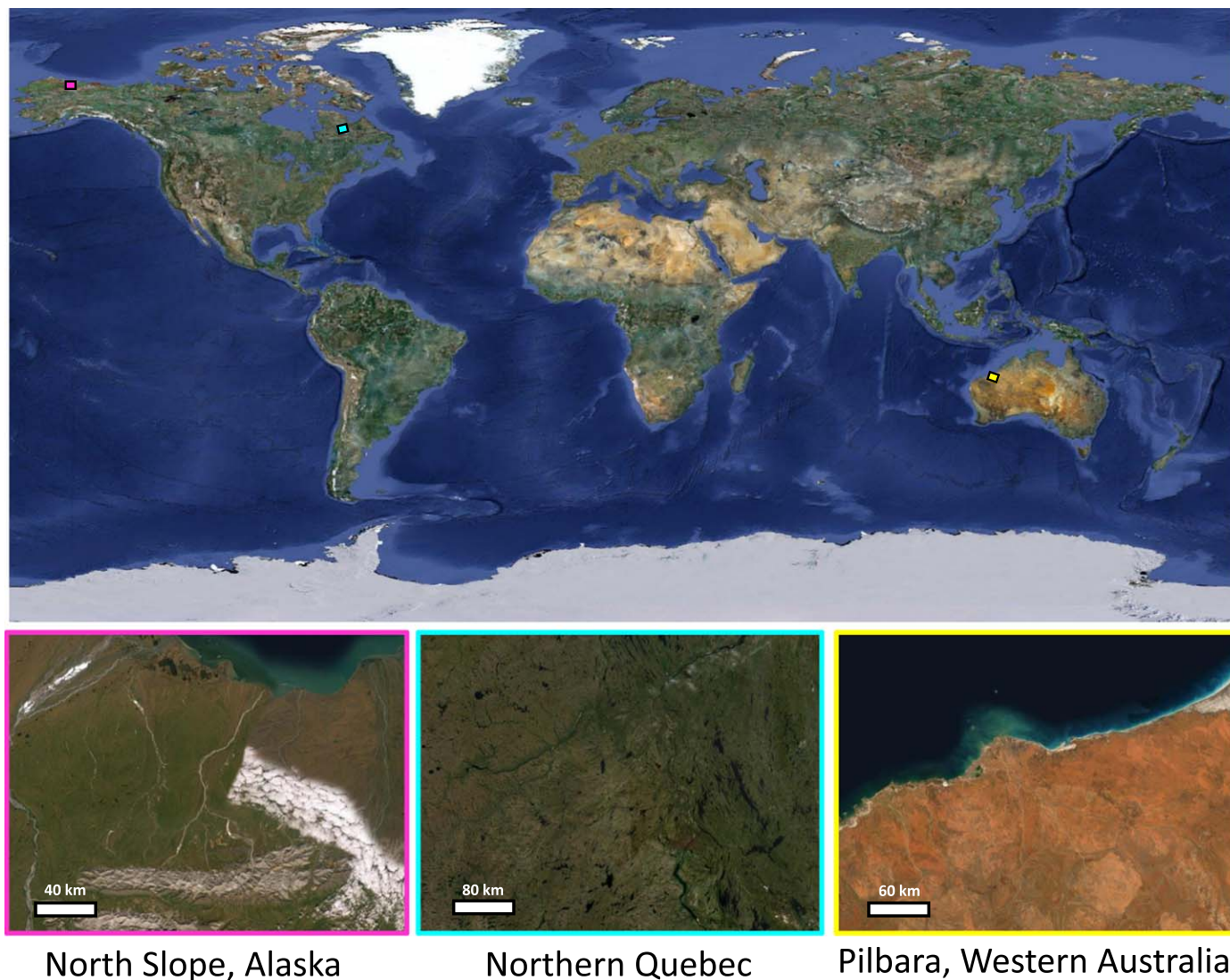
Figure 5. Top: global distribution of regions chosen for this study. Bottom: three SPOT images showing the full extent of the individual regions mapped. Coordinates (center of each image) from left to right: 69°49′31″N, 145°25′56″W; 57°40′59″N, 69°29′58″W; and 20°29′40″S, 119°35′30″E. The specific data used in this study are identified in Table A1.

terrestrial rivers comparable in size to those on Titan (>10 links visible at a resolution of $350\,\mathrm{m\,pixel}^{-1}$) that have not been substantially modified by humans and vegetation. Since K_u-band (and similar wavelengths such as C-band) radar data are highly sensitive to these effects (Elachi & van Zyl 2006), reducing the resolution of radar images in areas with major human influence and significant vegetation would not represent the degradation of vegetation-free terrain like that of Titan. With that said, we did try to find three large networks that may approximate different channels known on Titan, to investigate the effects of contrast and structural control.

The first region is in the Colville basin, in the eastern part of Alaska's North Slope Borough (pink in Figure 5). It is located just north of the Brooks Range, which formed during a compressional tectonic event during the early Cretaceous period (Nunn et al. 1987). The surface rock is sedimentary, ranging mostly between sandstone and shale (Mull et al. 2003), and the area was at least partially glaciated during the Pleistocene (Kaufman & Manley 2004). The region is currently covered in permafrost, and periglacial landforms, like thermo-karst lakes and pingos, are common (Walker et al. 1985). The

channels we map are located on a broad alluvial plain that extends to the Beaufort Sea, with a total relief of about 600 m.

The second region is in northern Quebec, on the Canadian shield (cyan in Figure 5). It has a total relief of approximately 400 m. It is on the border between the Superior and Churchill geological provinces in an area that formed between 1 and 3 billion years ago (Wardle & Van Kranendonk 1996). Rifting and orogenic activity during this time period (Wardle & Van Kranendonk 1996) likely resulted in fracture networks. The area is covered with discontinuous permafrost, and its topography has been altered significantly by glaciation, with the most recent retreat of the Laurentide Ice Sheet occurring around 10,000 yr ago (Occhietti et al. 2011).

The third region is on the northwest coast of western Australia (yellow in Figure 5). It is located on the Pilbara craton, a 3.5-billion-year-old formation composed of granite and greenstone that have undergone low-grade metamorphism and significant folding (Van Kranendonk et al. 2002). They are overlain in places by volcanic and sedimentary rock (Van Kranendonk et al. 2002). Pilbara has an arid climate with evaporation exceeding precipitation year-round, and what little
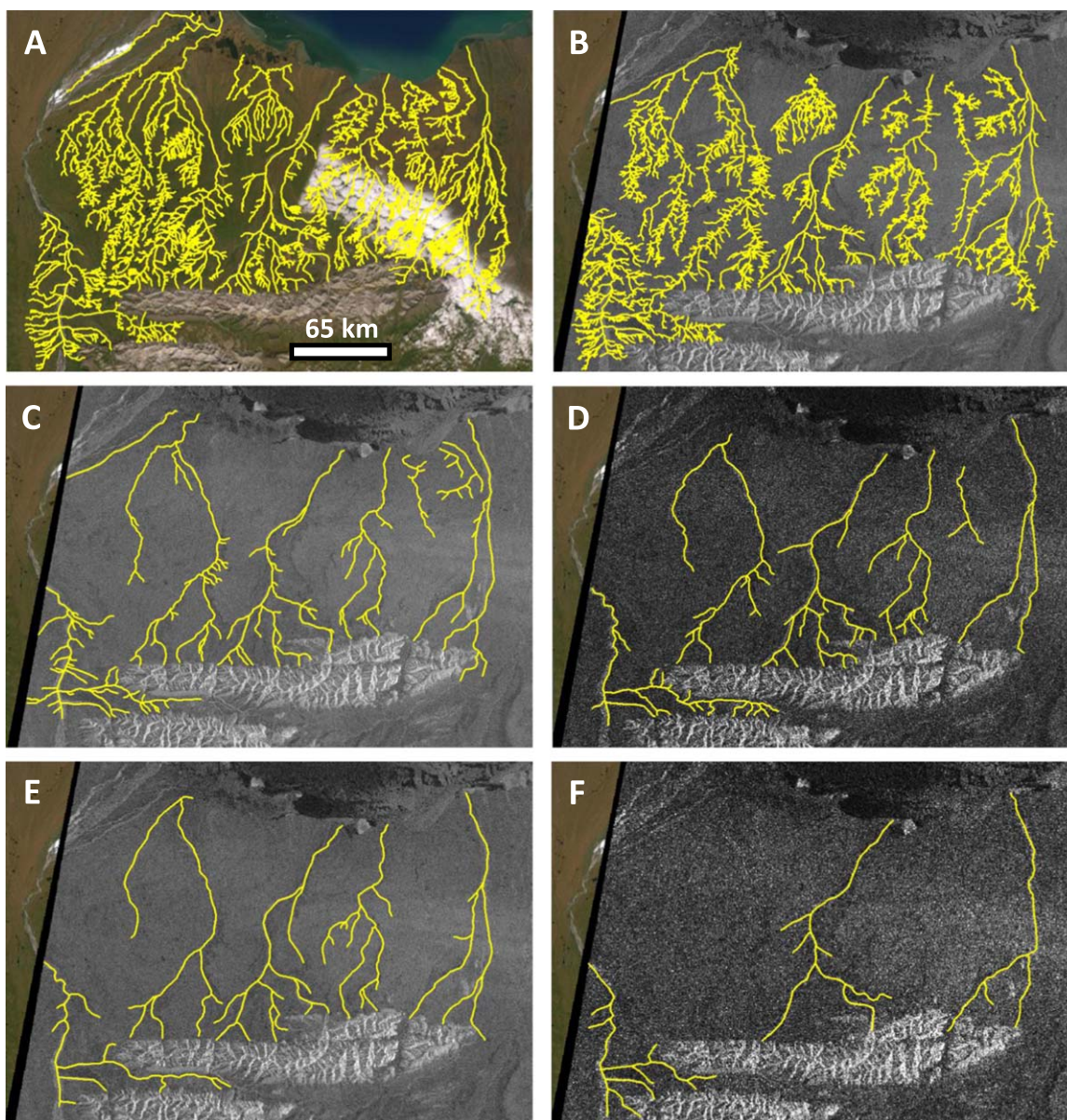
Figure 6. (A) Channels mapped from visible images with resolutions of 2.5 m pixel^{-1} in a select region of Alaska's North Slope. The cloud obscuring a portion of the right-hand side of the image was not present at the scale at which the channels were mapped. (B) Channels mapped from a 20 m pixel^{-1} SAR image of the same region. Channels mapped from the same SAR image degraded to 175 m pixel^{-1}, (C) without and (D) with speckle noise. (E) Channel map from the same SAR image degraded to 350 m pixel^{-1}. (F) Channel map from a "Cassini-quality" image: 350 m pixel^{-1} with speckle noise. See Figure A2 for an equivalent version of this figure without the channel mapping.

rainfall it gets typically occurs in the summer and fall (Sudmeyer 2016). Like in the North Slope mapping region, the mapped channels dominantly form on a broad alluvial plain that terminates in a delta, with a relief across the region of about 350 m. The majority of the channels mapped in this region were dry, likely ephemeral rivers.

3.2. Mapping Variations with Resolution

As would be expected, fewer channels were visible in lower-resolution images (Figure 6). The percentage of channels mapped at each resolution is given in Table 1. Those that remained visible at lower resolutions were generally wider and had higher backscatter with the surrounding terrain (see below).

3.2.1. High-resolution (2.5 m pixel^{-1}) Visible to High-resolution (10–30 m pixel^{-1}) SAR

Our first analysis is focused on variations that arise as a result of imaging with different wavelengths. SAR imaging, unlike visible imaging, senses the returned backscatter from the surface. This variation is broadly a function of the material properties, surface roughness, and large-scale slopes (Elachi & van Zyl 2006). For instance, vegetation appears bright in C-band radar images, as the vegetation canopy efficiently scatters incoming radar waves in all directions (Elachi & van Zyl 2006). Where vegetation was present in any of our mapped regions, it was mostly limited to areas near stream beds, resulting in some streams appearing brighter relative to their surroundings. Since the criteria for mapping channels included sinuous bright and dark features, such streams could be more
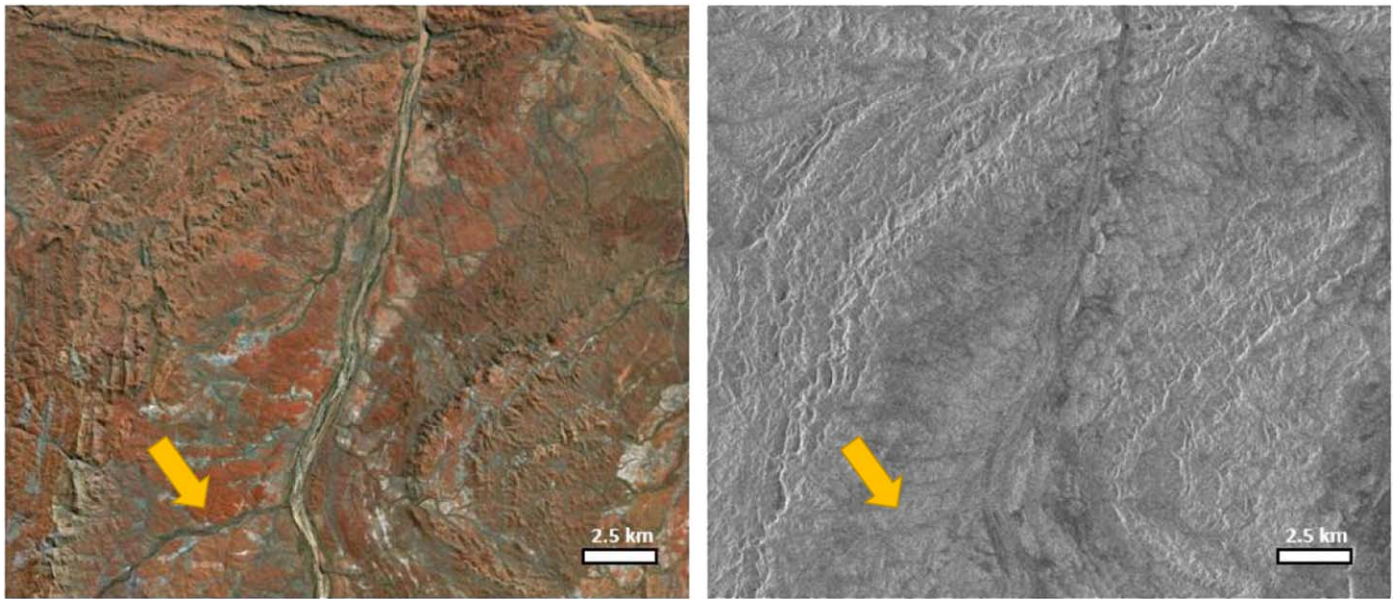
Figure 7. Left: part of a river network in Pilbara in a visible image with a resolution of 2.5 m pixel^{-1}; Right: the same network in a 10 m pixel^{-1} SAR image. The main branches can still be resolved in the latter, but less contrast with the surrounding terrain makes them difficult to map. Yellow arrows point to a channel link that can be seen clearly in the visible image but not in the SAR image.

Table 1
Changes in Percentage of Total Channel Length Mapped with Resolution

	Visible (2.5 m pixel^{-1})	High-resolution SAR (10–30 m pixel^{-1})	2× Cassini-quality SAR (175 m pixel^{-1})
Pilbara	100%	44.57%	8.62%
Quebec	100%	69.97%	21.25%
Alaska	100%	75.64%	15.12%

Note. The percentage of total channel length mapped at a given resolution changed with the quality of the images. We used the visible image data as a baseline, and so we list the percentage of channels mapped from these images as 100%. This format permits comparisons for the lower-resolution SAR data. We note that additional channels likely exist at smaller scales.

confidently mapped as channels. For example, channels that appeared to be narrow and filled in visible images appeared as wider, bright regions in SAR due to the vegetation along their banks. Small channels, which otherwise would not be observable in SAR, were therefore distinguishable owing to the presence of vegetation. This effect suggests that dry and/or narrow terrestrial channels would be somewhat more apparent in terrestrial SAR images than their counterparts on Titan, which do not have vegetation. As such, our conclusions about channel visibility obtained from Earth analogs would most likely constitute upper bounds. Despite our best efforts in selecting our mapping regions, this bias could not be entirely removed, meaning that the visibility of small channels is likely higher in terrestrial data than in Titan data of similar quality. Ideally, we would perform our analysis using SAR image data of channels on Mars, but such a data set does not exist.

Similarly, some dry braided stream networks were easily observable in SAR images, as their sediment-covered beds efficiently backscattered incoming radiation. However, there were also multiple instances where the channel bed and surrounding material were comparably rough. In these cases, the channels could clearly be seen in visible images but were

lost entirely in SAR images. This phenomenon was observed most dramatically in the Pilbara region (Figure 7), where large bright areas in the SAR indicated that the terrain was rough at the length scale of the radar wavelength. The streams in this region were mostly braided and were therefore indistinguishable from their mountainous surroundings in the SAR images. This loss was observed to occur even with channels substantially wider than 10 m across, so it is likely due to the wavelength and not the resolution.

This effect could conceivably also be an issue in areas with dry, sand-filled channels within smooth/flat terrains, where both would appear dark in SAR. However, a liquid-filled channel within a smooth terrain would likely still be visible owing to the significant differences in roughness between liquids and solids, even at Cassini-quality resolutions (Figure 3).

Even when channels were observed in both visible and SAR images, narrower channels and channels with similar reflective properties to surrounding areas were typically labeled with lower certainties. The loss of channels narrower than 1 pixel in the SAR data is attributed to the difference in resolution between the visible and SAR images.

3.2.2. High-resolution to Low-resolution Speckled and Unspeckled SAR

Substantially fewer channels could be mapped in both the low-resolution speckled and unspeckled SAR than in the high-resolution SAR, with the percentage of total links mapped in each region decreasing by a factor of 3–5 in each region. This loss of information was particularly significant in the Pilbara region, where dry or braided stream beds were common and the terrain near the channels was not heavily vegetated. These conditions resulted in a smaller difference in roughness between a channel and its surroundings, making radar-bright channels particularly difficult to map at low resolutions.

We observe that, when they are visible at all, channels with widths greater than 1 pixel in the downgraded but unspeckled SAR can be reliably mapped (or labeled with high certainty).
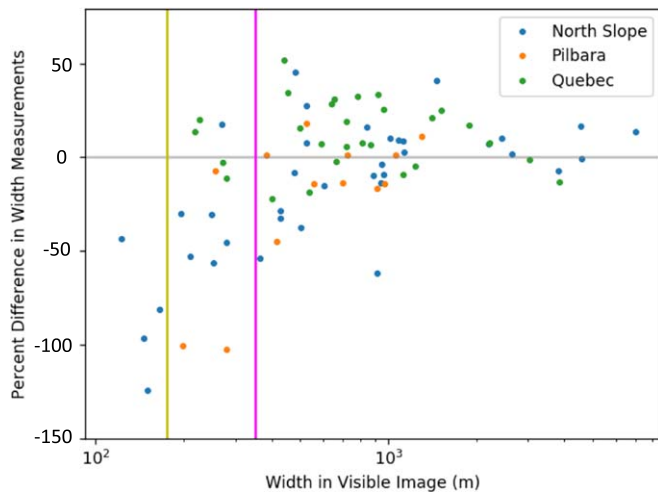
Figure 8. The discrepancy in width measurements made from visible and $2\times$ Cassini-quality images as a function of the channel's "true" (visible) width. The y-axis measures [(visible width)–(SAR width)]/(visible width). Negative values occur when the observed width is smaller than the width measured in the low-resolution image, so we are overmeasuring the channel's width in our low-resolution SAR mapping. The yellow line is at 175 m (1 pixel), and the magenta line is at 350 m (2 pixels).

Channels with widths smaller than 1 pixel can still sometimes be mapped, but these require greater contrasts to be visible and are less likely to be mapped with high certainty.

Channels wider than roughly 1.5 pixels are also consistently visible in the speckled data. Some smaller channels are also visible, but these are typically mapped with lower certainty.

3.3. Certainty

After channels mapped at $2\times$ Cassini resolution had been classified according to certainty, they were compared to channels mapped from high-resolution visible and SAR images. To determine how reliable our classification schemes were, we define a frequency that relates to whether rivers, mapped at $2\times$ Cassini resolution of a specific certainty class, physically existed in the location where we mapped them in higher-resolution data sets. We found that, across all networks, approximately 50% of low-certainty channels had physical counterparts in the high-resolution image data, while the other 50% consisted mostly of artifacts in the data and noise. Medium- and high-certainty channels corresponded much more frequently to physical channels, spatially correlating with real features 82% and 98% of the time, respectively. Further, the mapped medium- and high-certainty channels that did not have a 1-to-1 counterpart in high-resolution data sets were also less likely to be the products of noise. Instead, they tended to consist of areas where multiple channels from different networks or branches were close together and incorrectly mapped as continuations of the same channel, or where a real feature appeared to extend farther than it actually did.

3.4. Metrics

3.4.1. Width

Channel width was consistently overmeasured for the smallest channels at low resolutions when compared to widths from visible images (Figure 8). We hypothesize that this difference is because a channel resolved on a single-pixel scale in a low-resolution map might not take up the entire pixel.

Features adjacent to the channel, such as sloping banks, vegetation, and floodplains, were also mistaken for part of the channel in some cases at lower resolutions, although these features were typically narrower than 1 pixel. Channel width tended to be undermeasured at lower resolutions for larger channels, potentially because the edges of channels appeared less distinct in the low-resolution data. Note that we use the planform width as measured in the visible images as our baseline or "true" width for comparison with measurements made at lower resolution.

At widths greater than around 2 pixels ($\sim$700 m), the discrepancy in measured width between the visible and $2\times$ Cassini-quality images was typically less than 50%. This difference suggests that, for channels of this size, width can be measured reliably in low-quality images to within a factor of around two. This finding is consistent with the Rayleigh criterion often used to describe the minimum resolvable feature in visible images (Elachi & van Zyl 2006).

3.4.2. Minimum Drainage Area

Minimum drainage area was measured at all resolutions of visible and SAR data for all networks visible in the $2\times$ Cassini-quality images. It was found to increase by at most a factor of three for all terrestrial networks mapped, with a mean ratio of visible to low-resolution areas of 1.6 ± 0.5 (Figure 9).

3.4.3. Drainage Density

Drainage density was found to increase exponentially from low-resolution SAR to high-resolution SAR to the highest-resolution visible data. Drainage area increases slightly with better resolution since smaller channels at the edges of a network can be resolved, but better resolution also yields a more substantial increase in the total length of channels in a network: the mean ratio of total link length in visible to low-resolution maps was 7.2. On average, the calculated value for drainage density was 4.5 times lower for low-resolution data than for visible data. These data suggest that, for a network mapped from Cassini-quality images, the calculated drainage density would be consistently close to a minimum value.

3.4.4. Basin Aspect Ratio

Both drainage area and the length of the longest channel remained relatively constant with wavelength and resolution, with the latter changing by at most a factor of 2.5. The two measurements did not always change in a correlated manner, but the width/length ratio stayed fairly constant. The mean ratio of visible to low-resolution basin shape was 0.8, with a standard deviation of 0.3.

3.4.5. Junction Angle

By mapping two of the three separate regions three different times, we find that the average branching angles were accurate to within $\sim 2°$. The average branching angles of main network links were also computed for each network, and these were accurate to within $6°$.

When directly comparing the same junctions at different resolutions, the angles in the lower-resolution maps were on average higher, but there was a large spread in the data: the mean difference between low-resolution and visible angles was $8°$, and the standard deviation was $30°$.

Mapped from 2.5 mpp visible images	
Minimum Drainage Area	

Mapped from 10 mpp SAR images	
Minimum Drainage Area	

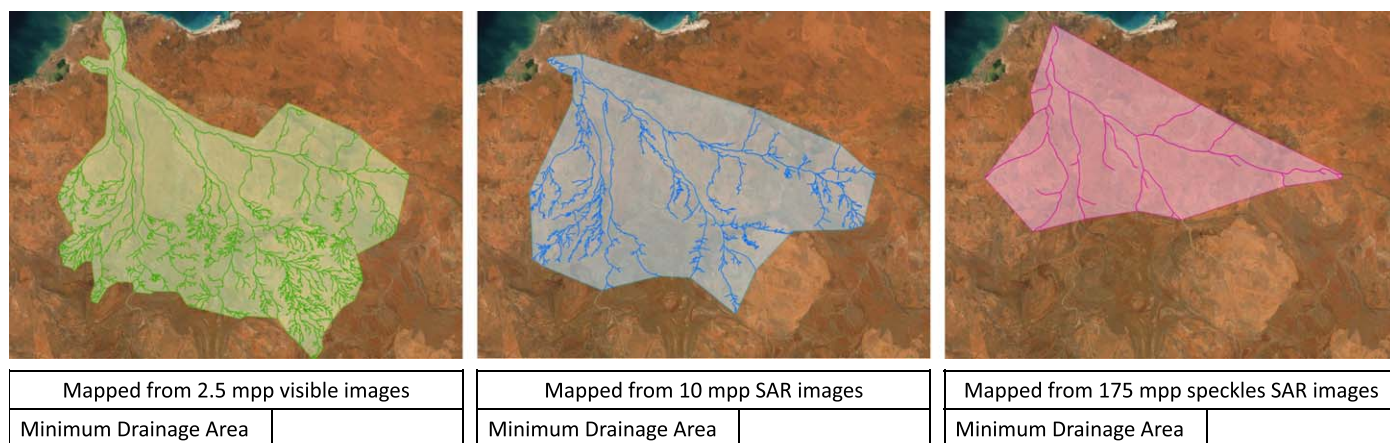| Mapped from 175 mpp speckles SAR images	
Minimum Drainage Area	

Figure 9. Mapped channels and minimum drainage area of the same network in Pilbara at different resolutions. The drainage area decreases by a factor of 1.7 between the highest-resolution visible and lowest-resolution SAR images.

We also averaged all junction angles measured in each network at each resolution, and this value was found to be greater in maps made from lower-resolution data. We hypothesize that this results from the selective loss of the smaller tributaries in the low-resolution data, which we observe, on average, to have smaller junction angles. This effect would act to skew the average junction angle in lower-resolution data to larger values.

Thus, while the mean difference may suggest that junction angles are minimally impacted by varying resolutions, the large errors and skew losses make extrapolating to lower resolutions unreliable. This suggests that the junction angles measured in the 2× Cassini-quality images would not accurately reflect the junction angles in a region on Titan.

3.4.6. Network Geometry

Although use of the adapted network classifications (Burr et al. 2013a) is reasonable given the quality of the data, the restriction to three geometries with no way to account for intermediate classifications makes this metric at best a useful approximation of morphology. As classification is highly dependent on metrics such as branching angle and total link length, which have been shown here to vary nonuniformly with resolution, the extent to which the classification at 2× Cassini quality is indicative of the actual surface morphology is therefore limited (Figure 10).

To test sensitivity, the same two networks in Alaska were mapped three separate times by the same individual. The networks from each map were then classified and compared. We observe that slight variations (within the large error bars) in branching angle and channel length when mapping the same network at the same resolution resulted in different classifications (Figure 11).

A significant factor in the network classification algorithm we used was the percentage of channels that came together at right angles (between 80° and 100°): a network with $\geq$20% angles would be considered rectangular regardless of its other characteristics. The number of right angles in both of these networks was found to vary by a few percent each time they were mapped. Because the number was near 20% in all cases, even slight variation in mapping meant that the same network could be classified differently.

Finally, changes with resolution in terrestrial networks did not display a clear pattern, although parallel networks did

become somewhat more common at lower resolutions. A larger-scale study would need to be conducted to determine whether the changes in network classification were significant. We therefore urge caution when applying automated classification schemes to Titan's channels, as the classification scheme is ill-suited to mapping results with large uncertainties.

3.4.7. Summary of Metrics

Drainage density and junction angle were found to be unreliable metrics for the purposes of this study, as both changed significantly with resolution. Junction angles were on average 8° higher for networks mapped from low-resolution images, with a wide standard deviation ($>$30°). Many smaller and narrower channels could not be mapped at all at low resolutions, so the average junction angle of a network would be artificially high. Drainage densities were on average 4.5 times lower. Network classification was strongly dependent on the measured junction angles and was observed to change inconsistently with resolution.

Drainage area and basin shape were both found to be less affected by the image resolution, which was also true for channel widths greater than 2 pixels. This finding means that width measurements on Titan greater than 700 m are likely to be relatively accurate. However, we note caution in our estimates of channel width, as they represent upper bounds given the lack of a priori knowledge as to the nature of the channel bed and floodplains, if present.

4. Titan Results

A preliminary investigation and mapping of Titan's channels were conducted by Burr et al. (2013a) using the Cassini SAR data collected through 2010, which covered about 40% of the surface (at $<$2 km resolution). An analysis was performed of the channel networks' geometries, flow directions, and geographic distribution. Using an automated network classification system, validated by using terrestrial networks, Burr et al. (2013a) determined that half of their mapped channels were rectangular and posited that this was the result of significant structural control.

Given our finding that network geometry was not a robust metric for Cassini-quality data, we chose not to classify networks on Titan. We instead focused on the metrics that we
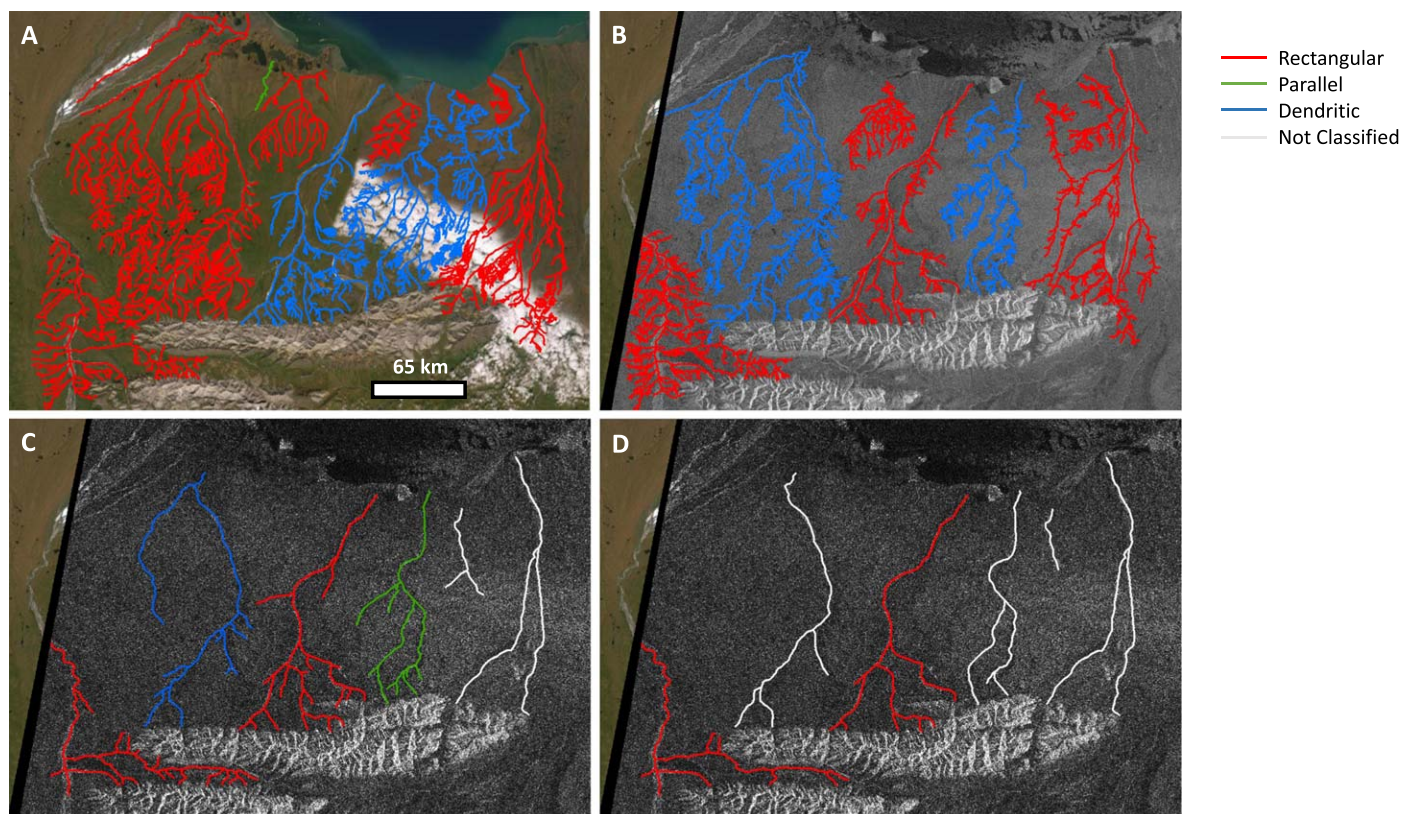
Figure 10. (A) Classification of networks mapped from visible images in the Colville Basin. Networks were mapped in the same location mapped on high-resolution SAR data (panel (B)), in 2× Cassini-quality SAR (panel (C)), and with only the high- and medium-certainty channels present (panel (D)). In panels (C) and (D), only networks with more than 10 links are classified; the remainder are shown in white. Channels deemed "unclassified" did not meet the requirements for any of the three potential geometries, though none of the networks in this region fell into that category. The white "Not Classified" channels contained fewer than 10 links, and classification was not attempted because it would not have produced statistically significant results (Burr et al. 2013a).

determined to be less sensitive to resolution: width, drainage area, and basin shape.

4.1. Geographic Distribution

The majority of Titan's channels imaged by Cassini are found in the polar regions and in the Xanadu region near the equator (Figure 12). Channels tend to be concentrated around large seas within the north polar region, with very few seen connecting or emptying into the smaller lakes. By contrast, channels in the south polar region were more widely and evenly distributed.

Further, channels mapped in the equatorial regions tended to be more uncertain than those mapped at the polar regions, and at the north polar region in particular. This observation could relate to the fact that polar channels are more likely to be liquid filled, providing a stronger contrast with the surrounding terrains. It is clear that the Xanadu region is highly dissected, but the paths of individual channels were generally difficult to discern (e.g., Moore & Pappalardo 2011; Burr et al. 2013a). This is consistent with our findings on the observability of channels within mountainous terrains (Figure 7), where radar-bright channels within a radar-bright mountainous region are difficult to discern, even with high-resolution SAR images.

The total length of channels, normalized by SAR coverage and corrected for the amount of SAR coverage at each latitude, is shown in Figure 13 (hereafter referred to as "channel clustering"). This is essentially a measurement of drainage density, and while we expect that the absolute values would not

be reliable, relative differences are more likely to still be meaningful.

The amount of channel clustering is high and relatively similar in both high polar regions (>80°), but there exists a significant dichotomy in density between the northern and southern portions of the polar (60°–80°), midlatitude (30°–60°), and equatorial regions (<30°).

Part of this dichotomy can be attributed to the fact that the sharp-edged depressions coincide with the latitudes of 60°–70° within the north polar region, which have been inferred to lack inflow/outflow channels (Hayes et al. 2008). Though sharp-edged depressions occur equally at both poles (Birch et al. 2017), there is a noted difference between the poles in coverage of mappable SAR image data (<1.5 km resolution). In the north, most of the "lake district" is well imaged, while there is a dearth of mappable SAR coverage over most of Kraken Mare, which extends toward 55°N. We also suspect that many channels that terminate into Kraken Mare may be missing, as the majority of the sea, which itself covers a substantial fraction of these latitudes, is poorly imaged. At the south, both the eastern and western hemispheres are equally covered in mappable SAR, though only half of the "empty basins" (Birch et al. 2018) are imaged.

Therefore, we hypothesize that some of the dichotomy, especially at ±50°–80°, can be attributed to coverage biases. However, despite the bias in SAR coverage between different portions of each polar region, there is another bias that makes mapping channels at the north comparably easy. Specifically, the observed channels draining into the seas at the north are
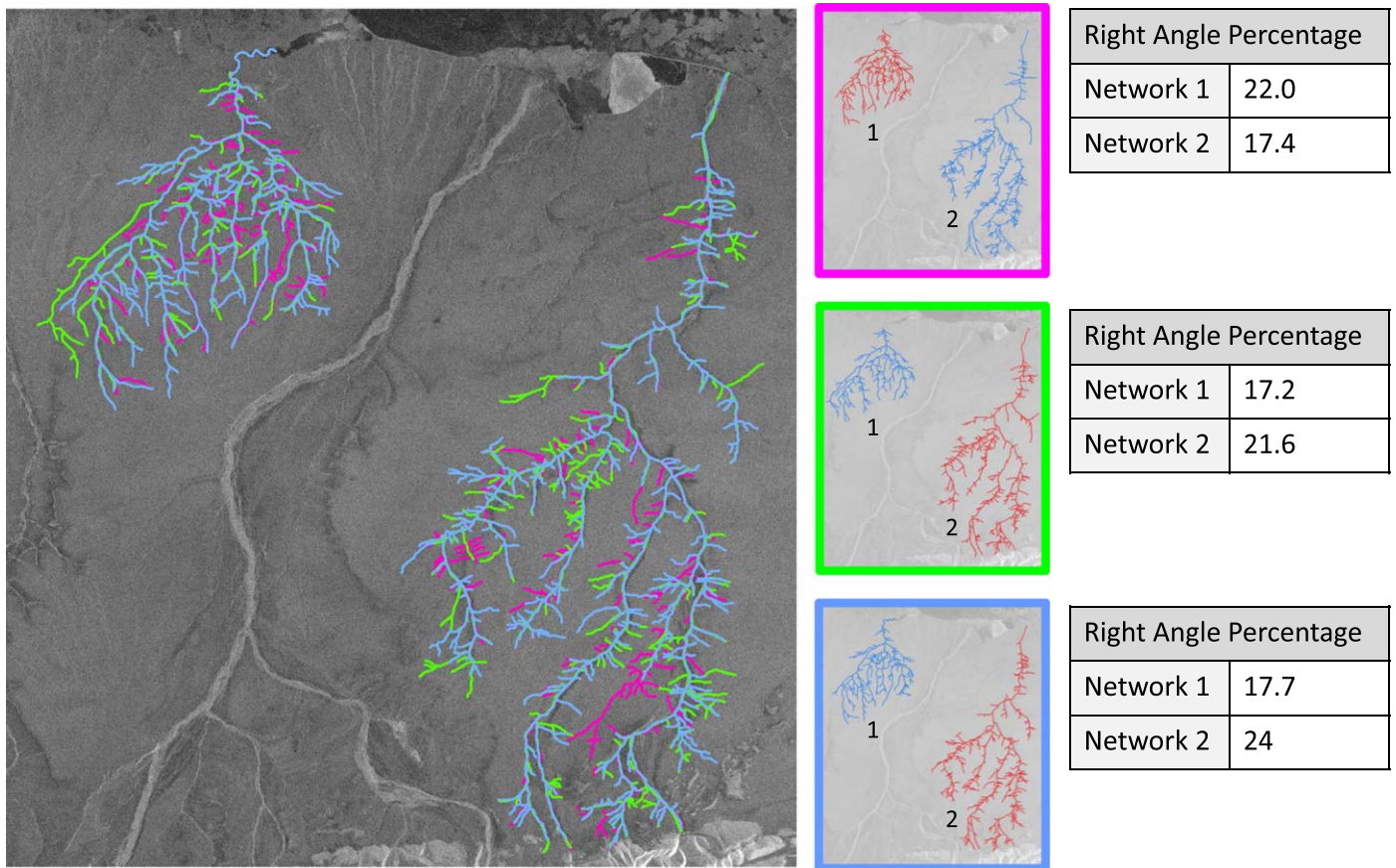
Figure 11. Three separate mappings (each in a different color) of the same two networks in the North Slope region from 20 m pixel^{-1} SAR (left panel) (69°50′56″N, 145°09′12″W). The classification of each network is shown for each mapping (in boxes of corresponding color) on the right, where blue is dendritic and red is rectangular. To be rectangular, at least 20% of a network's junctions must be right angles (between 80° and 100°).

liquid filled and flooded, making them easy to discern from their surroundings. We suspect that there may be unobserved channels at the south that drain into the equally large empty basins, likely because they are not flooded and therefore not artificially widened. The southern channels may also be dry, and if their channel beds are smooth sand, they would be equally unobserved within the SAR-dark plains through which they flow.

The higher degree of clustering of low-latitude channels in the southern hemisphere is not solely tied to Xanadu, which ranges from 15°N to 30°S (Radebaugh et al. 2011). There are a greater number of channels from 40°S to 60°S that have no relation to Xanadu or the polar regions. As there is similar or greater SAR coverage at the equivalent northern latitudes, this dichotomy is likely a property of Titan's surface (e.g., relief, "rock type" favorable for channel formation, etc.), and not related to coverage biases. Since the high-relief region of Xanadu has a particularly high rate of channel clustering, it seems likely that the dichotomy results partially from differences in relief.

4.2. Comparison with Previous Results

When conducting this study, we had access to data sets with greater coverage and higher resolution than were available for previous studies (Jaumann et al. 2008; Lorenz et al. 2008; Burr et al. 2009; Lopes et al. 2010; Langhans et al. 2011; Burr et al. 2013a), and comparisons with earlier maps reflect these differences. There were some features such as raised lake rims

that appeared channel-like at lower resolution (Burr et al. 2013a), but which we were able to determine were not channels because of newer, often higher-resolution data sets and the fact that we relied on individual SAR swaths instead of layered mosaics (Figure 14). There were also several newly imaged areas that contained channels and areas where better image quality revealed new channels.

4.3. Titan Metrics

4.3.1. Width

Average width was measured along a 5–25 km long section of each channel that was clearly radar-dark or radar-bright, but not for channels with a bright-dark pairing. In the latter case, it would not have been possible to distinguish valley width from the physical width of the channel. Though not always the case, radar-dark channels in terrestrial SAR data tend to correspond to realistic physical widths, either of the channel itself or of the channel and its immediate floodplain. Further, radar-bright channels tended to correspond to the width of gravel beds of dry or braided rivers, and so we assume that such channels on Titan indicate similar features and can reasonably be compared. Figure 15 shows the width distribution of all bright and dark channels on Titan whose widths were most likely to correspond to bankfull width.

Whereas data sets do exist for the distribution of terrestrial channel widths, differing definitions of channel widths make a direct comparison difficult (e.g., Yamazaki et al. 2014). Given
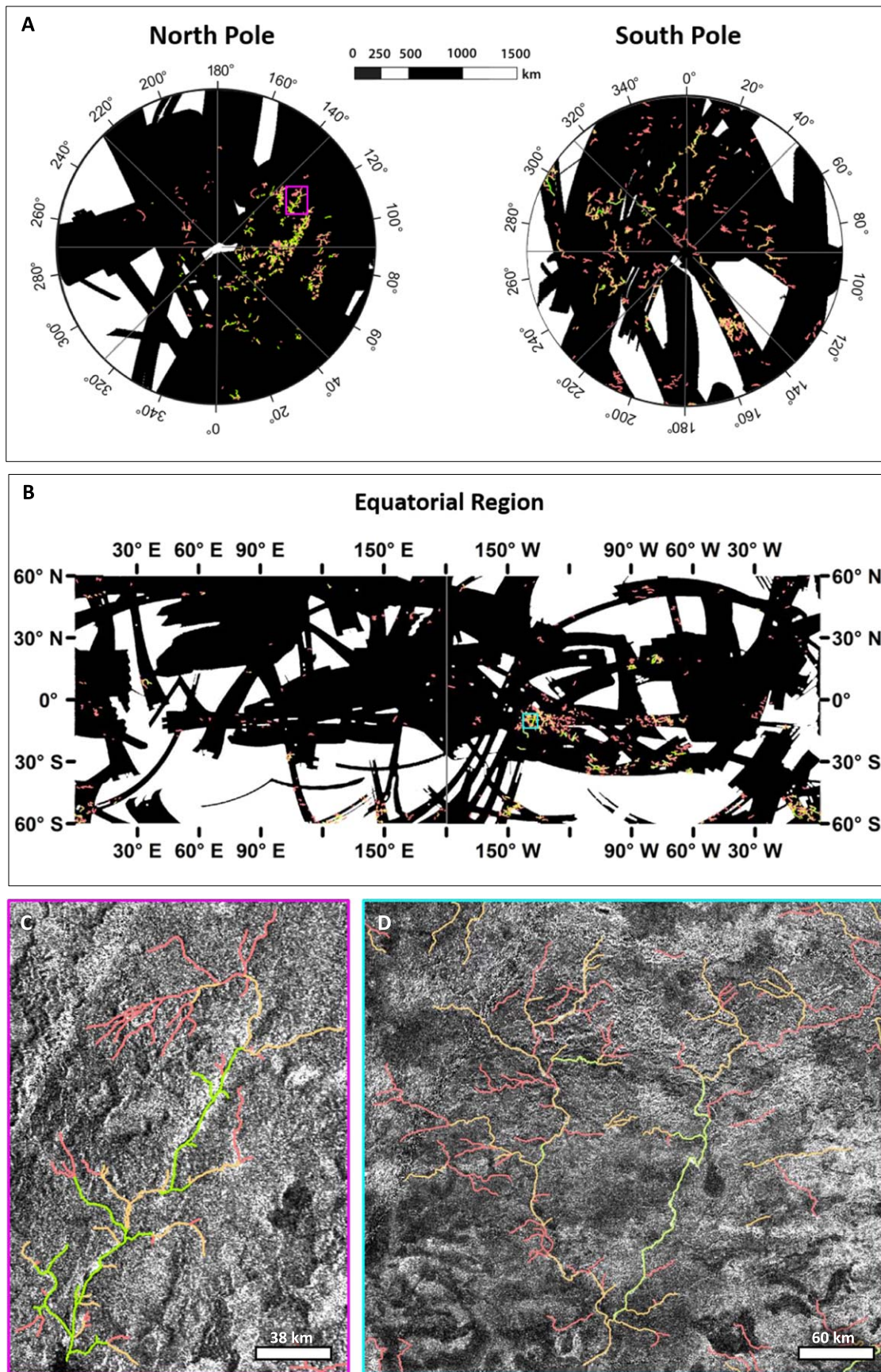
14

Figure 12. (A) Polar stereographic view of mapped channels at latitudes greater than ±60° for both the North and South. (B) SAR coverage and channels in the equatorial region, between 60°N and 60°S. The pink and teal boxes in these views correspond to the detailed maps of (C) Vid Flumina (north polar river, 72°54′N, 242°15′W) and (D) a river network in Eastern Xanadu (equatorial river, 9°29′S, 139°14′W). Channel segment color corresponds to certainty, with green being most certain and red being least certain. The full maps are provided as shapefiles and are made available with this work.
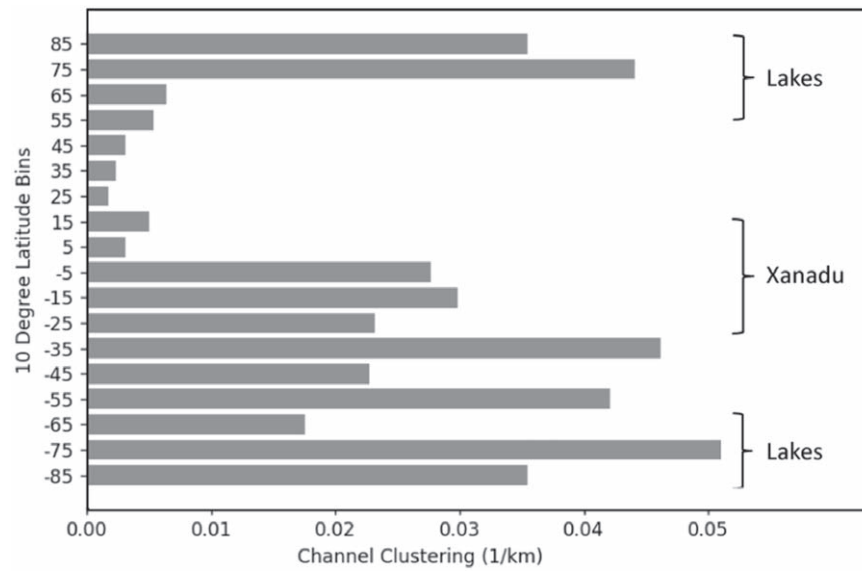
Figure 13. Variability of channel clustering with latitude on Titan. Channel clustering was found by calculating the total length of all channels in each latitude bin and dividing by the area covered with Cassini SAR. The numbers on the *y*-axis denote the centers of the bins.
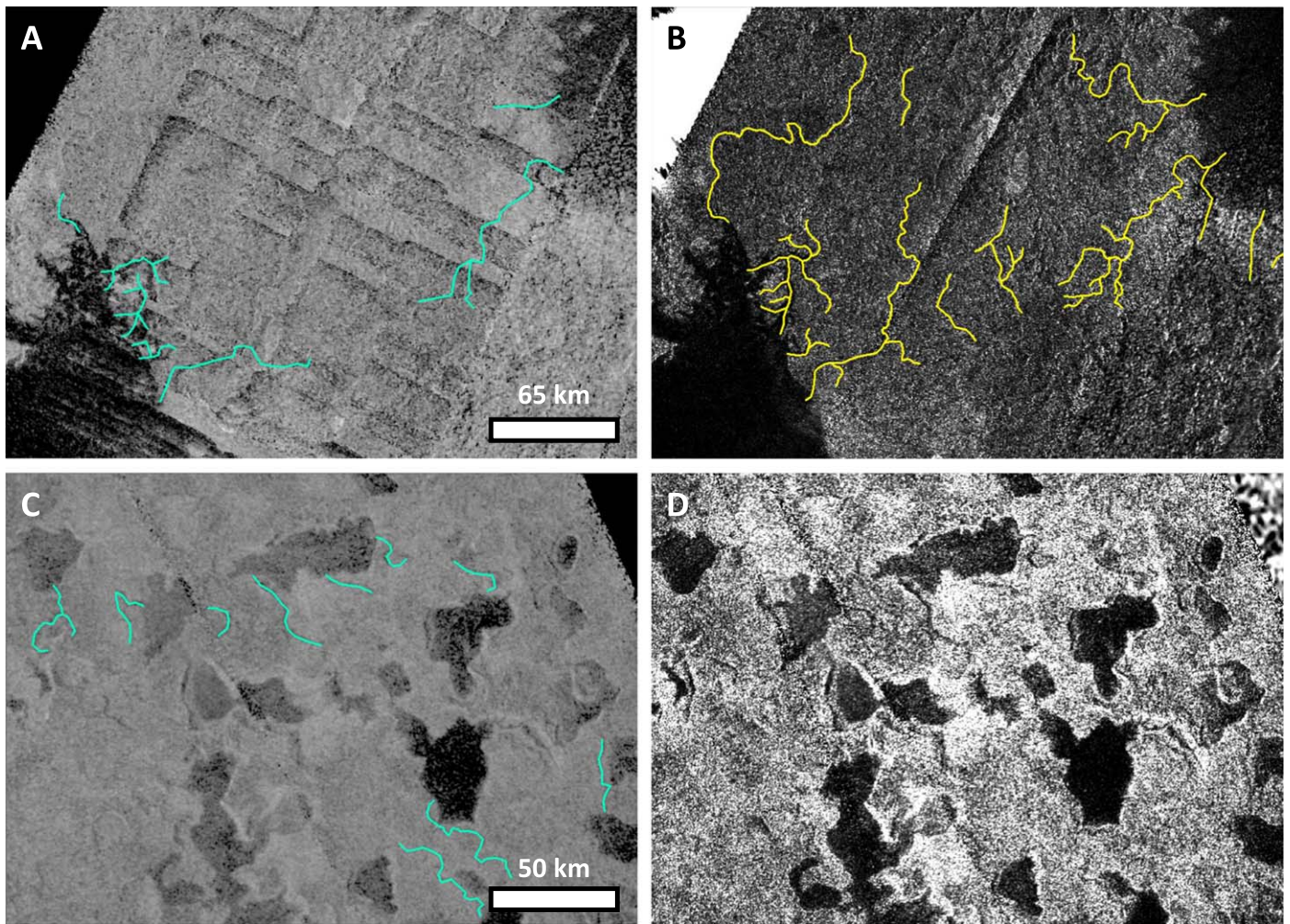
Figure 14. (A) and (C) Channel maps produced by Burr et al. (2013a) with the SAR data used for that study. (B) and (D) Our maps with the end-of-mission SAR data. Panels (A) and (B) show the same area between Ligeia Mare, Kraken Mare, and Punga Mare, where more channels were able to be mapped from later, higher-quality swaths. Panels (C) and (D) show a portion of the "lake district" at the north polar region, where features mapped as channels by Burr et al. (2013a) are interpreted here as the raised rims of sharp-edged depressions (Birch et al. 2019).
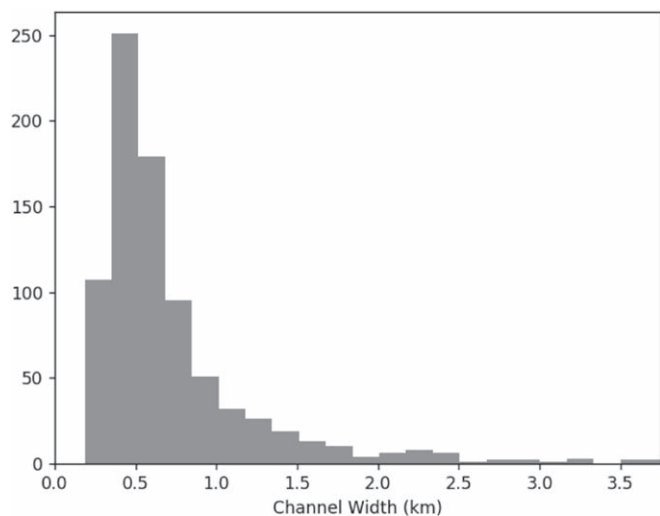
Figure 15. Counts in 167 m bins of all bright and dark channel widths measured on Titan. This plot excludes the 10 channels mapped with widths >3.75 km; the widest of these is 10 km.

Figure 16. Comparison of the distribution of basin shapes at the poles (poleward of 60°) with that at the equator (from 60 N to 60 S).

this uncertainty and the resolution limits of the Cassini SAR data, we choose not to compare channel widths between Titan and Earth.

One additional complication exists for the SAR-dark channels on Titan, found almost exclusively flowing into seas at the north polar region. There are some indications that these are actually valleys drowned owing to sea level rise and not actively flowing river channels (Stofan et al. 2007; Hayes 2016). Apparent changes in channel width along these features could instead be variations in valley width at a given elevation contour. Thus, the measured channel widths of the drowned north polar rivers may be overestimates.

The small population of very wide (>2 km) channels is composed of these potential flooded valleys at the north pole and of the >1000 km long, radar-bright features in the equatorial region (Figure 12). The decreased count of channels with widths smaller than 334 m is likely due to the resolution and image quality of the data: channels narrower than this value are difficult to map confidently and consistently. The majority of mapped channels with such narrow widths were radar-dark features at the north polar region. The substantially lower roughness of dark linear features (in addition to a higher backscatter contrast) likely makes them easier to distinguish even when they are at lower resolution. The 0.334–0.500 km width bin is similarly thought to have an artificially low count.

Finally, in regions where overlapping swaths showed the same channels observed at different dates, the widths of these channels did not appear to differ appreciably based on our first-order analysis.

4.3.2. Minimum Drainage Area

Minimum drainage area was measured for all networks with at least 10 links. The average minimum drainage area at the equator was around 1800 km^2, substantially higher than at the poles. The average in the north polar region was around 300 km^2, and the average in the south polar region was around 700 km^2. Drainage area varied substantially in all regions, with standard deviations comparable to the mean values, consistent with our terrestrial mapping.
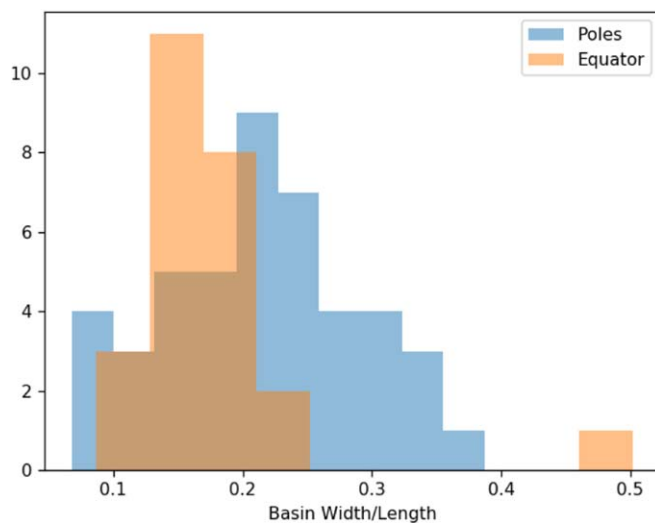
4.3.3. Basin Aspect Ratio

Basin aspect ratio was determined for all networks with at least 10 links (Figure 16). The width/length ratio at the polar regions was both significantly broader and higher than that at the equator; the polar regions were not compared individually because their differences were not statistically significant.

5. Discussion

Based on terrestrial results, measurements of drainage density and average junction angle from SAR (including those of Cassini data of Titan) are unlikely to accurately reflect observations using visible imagery but would represent lower and upper limits, respectively. Calculations of drainage density made from high-resolution (<50 m pixel^{-1}) data, such as what might be acquired by Dragonfly, would provide more information on the influences of fluvial and erosional processes on Titan, particularly those of Titan's hillslopes (Lorenz et al. 2018). The near-minimum drainage densities calculated from Cassini SAR data do not permit meaningful conclusions to be made about such processes, so we do not discuss our results further.

On Earth, we frequently find that high- and medium-certainty channels mapped from Cassini-quality data correspond to real fluvial features (>98% and 82% of the time, respectively), and that minimum drainage areas for mapped networks of these certainties are relatively accurate at the ~1 km scale.

Channel width measurements >700 m are likely accurate to within a factor of two for channels on Titan. The counts for such channels are also expected to be relatively close to true values for regions with high-quality (<350 m pixel^{-1}) SAR coverage. We posit that a substantial number of wide (>700 m pixel^{-1}), filled channels went unmapped where mappable SAR coverage was unavailable, since these channels are particularly visible in SAR data. This type of channel was also seen almost exclusively near the seas at the north polar region—a region that was imaged well around Ligeia Mare, but sparsely around Kraken Mare and Punga Mare.

There is also a greater possibility that braided channels or dry channel beds could not be seen even when wide enough to

be detected, because the roughness of the channel bed was too similar to that of the surrounding terrain. This effect was seen in Pilbara, Australia, where many wide channel beds in unvegetated, gravelly areas could not be seen in SAR images (Figure 7). Similarly, many dry, sand-bedded channels were likely missed by Cassini SAR if they were embedded within radar-dark terrains, of which there are numerous examples across Titan (e.g., midlatitude plains and equatorial dunes).

A difference in weathering rates due to differences in substrate material between the poles and equator may explain the relatively wider basins at Titan's poles. In such a scenario, we posit that weathering rates of polar materials are significantly higher, allowing surface material to be broken down more easily on hillslopes. This would result in a net widening of polar basins, compared to their respective lengths. This hypothesis would also be consistent with previous work suggesting the presence of vast organic deposits at the polar regions (Birch et al. 2016; Neish et al. 2016), which are assumed to be erosionally weaker than water ice.

Additionally, as described by Black et al. (2012), the more humid climates of Titan's polar regions may have promoted more extensive erosional dissection of the terrain by fluvial networks. This would be corroborated by our observed distribution of channel clustering with latitude, where we find more channels at higher latitudes. In the Black et al. (2012) model, river basins first start out long and narrow and, as they compete for drainage area, widen as the landscape gets more thoroughly dissected. Thus, whether due to increased weathering rates from lithologic differences, due to time and the erosional history of the landscape, or a combination of the two, our basin aspect ratio results are consistent with measures of the width function by Black et al. (2012) and suggest that Titan's polar regions are more dissected than lower latitudes.

One surprising observation is the difference in channel density between the northern and southern equatorial zones. While we expect that the equatorial channel density should be clearly lower, we also expected it to be symmetric about the equator. To explain this difference, we suspect that the large relief near the equator in the southern hemisphere, dominated by the mountainous Xanadu region, may play a role. Channels are more likely to be clustered in areas with greater relief, and channel clustering is accordingly greater in areas such as Xanadu. The near-complete dearth of channels in the midlatitudes may similarly be attributed to a lack of relief. The only observed channels are around local, small-scale topographic features, with the remainder of the region dominated by the vast undifferentiated plains (Lopes et al. 2020).

An additional factor was our decision not to map channels within Titan's enigmatic labyrinth terrains (Malaska et al. 2020). These terrains appear highly dissected, but by valleys showing clear radar-bright/radar-dark pairing, with few visible channels. Though mapping may be performed, we found that our maps were unable to produce consistent results: unfilled channels were narrower than 2 pixels on most occasions, and there was not a substantial roughness or dielectric contrast with the surrounding terrain. As the labyrinth terrains are mostly located at the polar regions, we suspect that our polar numbers may be deflated, particularly at the south, which has a larger fractional coverage of labyrinth terrains (see Malaska et al. 2020, Figure 7 in text).

The north polar region is also characterized by two general terrains on each of its hemispheres: the small lakes and the larger seas (Birch et al. 2017). The area of small lakes does not contain any visible channels at the available SAR resolution and is morphologically consistent with formation proposed through karstic dissolution (Hayes et al. 2017), whereas the seas (which have visible channel networks flowing into them) cover a vast fraction of the remaining region. Both factors will suppress the total channel density.

Finally, we recognize that we are unable to map all the channels on Titan and there are likely a large number below Cassini's resolution (e.g., Moore & Pappalardo 2011; Burr et al. 2013a). However, to first order we would expect that Dragonfly would observe more channels within proximity to the high-relief Selk crater rim than within hummocky terrains of the ejecta blanket surrounding the crater (e.g., as the terrains imaged by Huygens). Given a relatively large exploration distance (~1000 km), a sufficiently large range of latitudes may be covered, in which case we might see variation in drainage basin aspect ratio. If Dragonfly were to pass over any of the radar-bright channels, we expect that it would observe a clearly defined braided channel and/or gravel-bedded river, consistent with previous interpretations (Lorenz et al. 2008; Burr et al. 2013a). We could then compare Dragonfly's measured width to Cassini's. A comparison of how width scales as a function of resolution on both Titan and Earth would then enable us to then investigate whether any sub-Cassini-resolution properties of Titan's channels differ from Earth's.

6. Conclusion

Terrestrial fluvial geomorphology is typically studied with the aid of topographic data and high-resolution visible images of the areas of interest (Dietrich et al. 2003), neither of which is available at sufficient resolutions on Titan. Although the quality and quantity of Cassini SAR images put significant limits on their utility for investigating river networks, they can still be used to understand Titan's landscape at a fundamental level (Black et al. 2012; Tewelde et al. 2013).

We used Earth data to determine what could be learned from planform images with significant noise and low spatial resolution. We found that the traditional metrics of drainage density and junction angle were not reliable in these circumstances and that uncertainties in these areas can lead strict classification systems for network geometry to produce ambiguous results. However, other metrics such as a minimum drainage area, basin aspect ratio, and channel width were still relatively accurate.

We applied these three reliable metrics to the channels visible in the Cassini SAR data. We were able to measure the widths of channels >700 m with relative accuracy (to within a factor of two) and to observe the distribution of all measured widths. We found the drainage areas and basin shapes of large (>10 links) networks and investigated systematic changes with latitude. The polar regions had wider basins and a greater degree of channel clustering, suggesting that they are more humid and/or have more friable rock than the equator. We also observed a significant dichotomy in channel clustering at the midlatitudes, which is thought to result at least partially from differences in topographic relief.

We expect observed trends on Titan to continue at smaller scales and to be confirmed by Dragonfly and other future missions. Dragonfly's collection of higher-quality visible data

will additionally permit Titan's surface to be studied on a finer scale, using advanced higher-resolution geomorphological analysis.

Appendix A
Interpretation of Cassini Sar Data

Figure A1 shows a map of spatial resolution for Cassini RADAR data, which ranges from around $250\,\mathrm{m\,pixel^{-1}}$ to $100\,\mathrm{km\,pixel^{-1}}$. Figure A2 shows how incidence angle information for a given SAR swath can be used to determine whether a linear feature is a ridge or valley. All mapping products created in this study can be found at https:// hayesresearchgroup.com/data-products/.
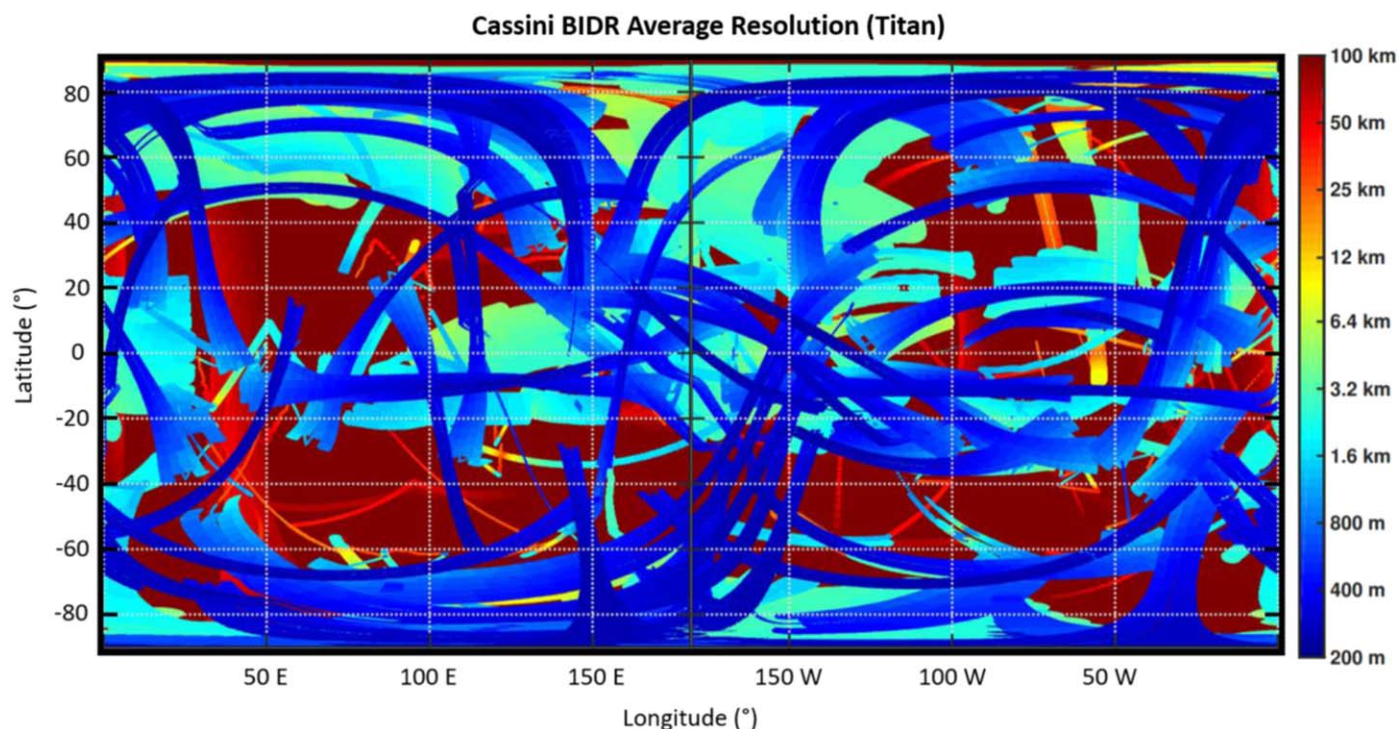

Figure A1. Map of spatial resolution for Cassini RADAR Basic Image Data Record (BIDR) data, which consist of SAR, HiSAR, and scatterometry data sets. The scatterometry data set covers the entire moon with spatial resolutions between 10 km and $100\,\mathrm{km\,pixel^{-1}}$, and while it is useful for determining surface roughness and terrain type over very large scales, the data are too coarse for fluvial features to be identified. HiSAR was obtained when the spacecraft was more than 10,000 km from the surface of Titan, and the resolution of the data ranges between 1 and $5\,\mathrm{km\,pixel^{-1}}$. The SAR data set has the most limited coverage but the highest resolution, which ranged between 250 and $500\,\mathrm{m\,pixel^{-1}}$. This was the data set in which the vast majority of Titan's channels could be seen. More information on the Cassini RADAR instrument and its data products can be found in Wall et al. (2019).
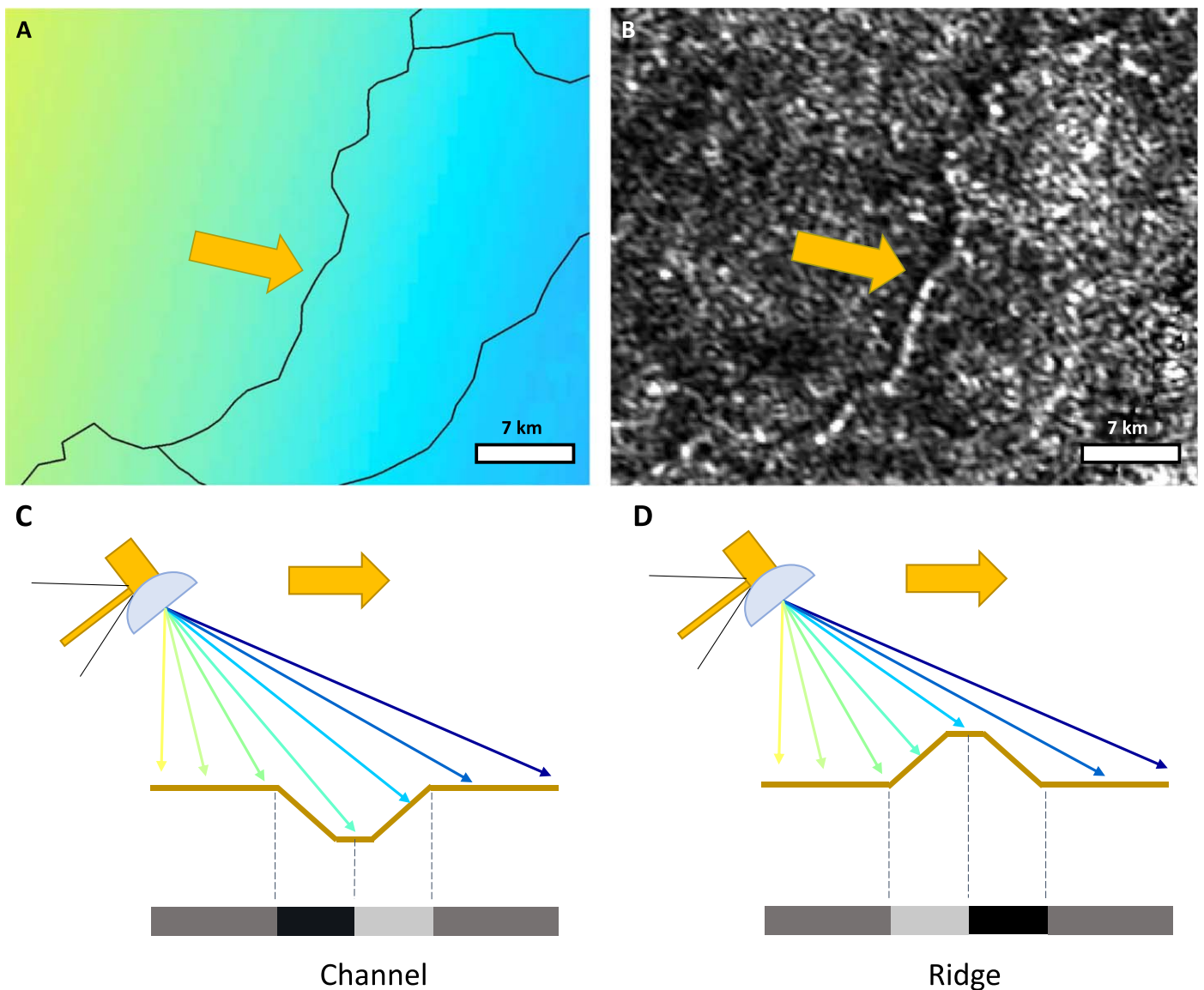
Figure A2. (A) Map of incidence angles for a swath of Cassini SAR data, with more yellow corresponding to smaller angles. The orange arrow points from low to high incidence angle, indicating look direction for the swath. The overlaid black lines represent mapped channels. (B) Cassini SAR for the same area. The central linear feature was determined to be a channel, rather than a ridge, because the feature is dark and then bright with increasing incidence angle. (C) and (D) Differences in topography are reflected in the different pixel values along a cross section of each feature. The latter represents the situation in panel (A).

Appendix B
Terrestrial Data

Figure B1 shows our region of study in Alaska at various resolutions, as a parallel to Figure 6. Table B1 describes the

radar data used in the terrestrial portion of this study, including their dates and IDs. All visible images used in this study are part of the ESRI World Imagery Basemap.
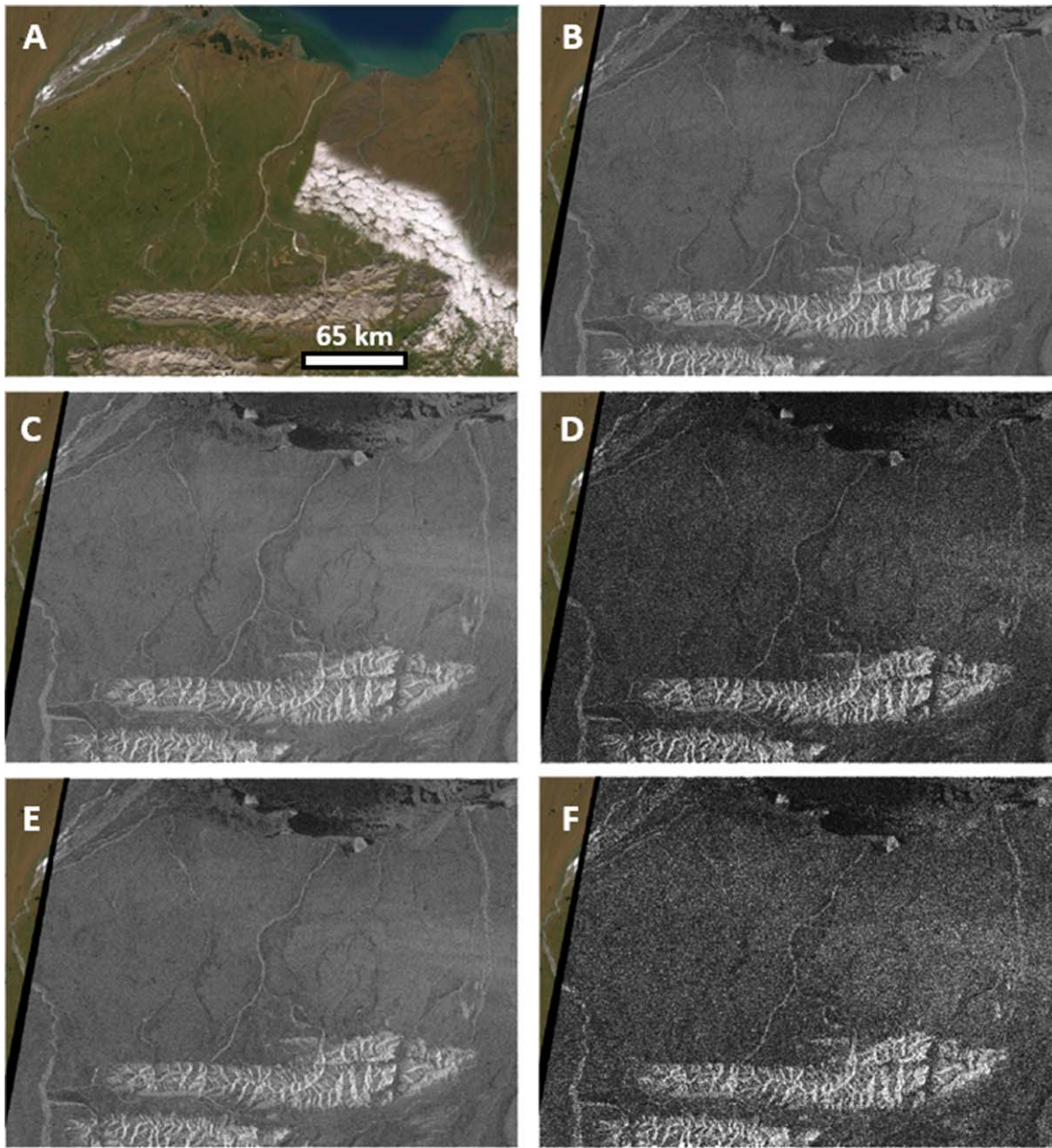
Figure B1. (A) Visible images with resolutions of 2.5 m pixel^{-1} in a select region of Alaska's North Slope. The cloud obscuring a portion of the right-hand side of the image was not present at the scale at which the channels were mapped. (B) 20 m pixel^{-1} SAR image of the same region. The same SAR image degraded to 175 m pixel^{-1}, (C) without and (D) with speckle noise. (E) The same SAR image degraded to 350 m pixel^{-1}. (F) "Cassini-quality" image: 350 m pixel^{-1} with speckle noise.

Table B1
The Sentinel-1 Data Used in This Study

Sensing Date	Northern Alaska 2017-10-24	Northern Quebec 2017-09-07	Western Australia 2018-06-27
Identifier	S1A_IW_GRDH_1SDV_ 20171024T161020_ 20171024T161049_ 018957_020098_4B11	S1B_IW_GRDH_1SDV_ 20170907T222145_ 20170907T222214_ 007292_00CDC9_4991	S1B_IW_GRDH_1SDV_ 20180627T213055_ 20180627T213124_ 011564_01541D_2CAE

ORCID iDs

S. P. D. Birch ⓘ https://orcid.org/0000-0002-4578-1694
M. J. Malaska ⓘ https://orcid.org/0000-0003-0064-5258
R. M. C. Lopes ⓘ https://orcid.org/0000-0002-7928-3167
P. M. Corlies ⓘ https://orcid.org/0000-0002-6417-9316

References

Abrahams, A. D. 1984, WRR, 20, 161
Birch, S. P. D., Hayes, A. G., Corlies, P., et al. 2018, Icar, 310, 140
Birch, S. P. D., Hayes, A. G., Dietrich, W. E., et al. 2017, Icar, 282, 214
Birch, S. P. D., Hayes, A. G., Howard, A. D., Moore, J. M., & Radebaugh, J. 2016, Icar, 270, 238
Birch, S. P. D., Hayes, A. G., Poggiali, V., et al. 2019, GeoRL, 46, 5846
Black, B. A., Perron, J. T., Burr, D. M., & Drummond, S. A. 2012, JGRE, 117, E08006
Black, B. A., Perron, J. T., Hemingway, D., et al. 2017, Sci, 356, 727
Brown, M. E., Bouchez, A. H., & Griffith, C. A. 2002, Natur, 420, 795
Buono, A., Nunziata, F., Migliaccio, M., Yang, X., & Li, X. 2017, IJRS, 38, 6714
Burr, D. M., Drummond, S. A., Cartwright, R., Black, B. A., & Perron, J. T. 2013a, Icar, 226, 742
Burr, D. M., Jacobsen, R. E., Roth, D. L., et al. 2009, GeoRL, 36, L22203
Burr, D. M., Perron, J. T., Lamb, M. P., et al. 2013b, GSAB, 125, 299
Cabrol, N. A., & Grin, E. A. 2001, Geomo, 37, 269
Chang, H. H. 1980, J. Hydraul. Div. Am. Soc. Eng, 106, 1443
Dietrich, W. E., Bellugi, D. G., Sklar, L. S., et al. 2003, in Prediction in Geomorphology. Geophys. Monogr. Ser., Vol. 135, ed. P. R. Wilcock & R. M. Iverson (Washington, DC: AGU), 103
Dunne, T., & Leopold, L. 1979, Water in Environmental Planning (San Francisco: Freeman)
Elachi, C., & van Zyl, J. 2006, Introduction to the Physics and Techniques of Remote Sensing (2nd ed.; Hoboken, NJ: Wiley), 341
Faulk, S. P., Lora, J. M., Mitchell, J. L., & Milly, P. C. D. 2020, NatAs, 4, 390
Griffith, C. A., Owen, T., Miller, G. A., & Geballe, T. 1998, Natur, 395, 575
Hayes, A., Aharonson, O., Callahan, P., et al. 2008, GeoRL, 35, L09204
Hayes, A. G. 2016, AREPS, 44, 57
Hayes, A. G., Birch, S. P. D., Dietrich, W. E., et al. 2017, GeoRL, 44, 11,745
Horton, R. E. 1945, GSAB, 56, 275
Howard, A. D. 1967, BAAPG, 51, 2246
Ichoku, C., & Chorowicz, J. 1994, WRR, 30, 161
Jaumann, R., Brown, R., Stephan, K., et al. 2008, Icar, 197, 526
Kaufman, D. S., & Manley, W. F. 2004, Developments in Quaternary Sciences, 2, 9
Klemenjak, S., Waske, B., Valero, S., & Chanussot, J. 2012, IJSTA, 5, 1364
Langhans, M. H., Jaumann, R., Stephan, K., et al. 2011, P&SS, 60, 34
Le Gall, A., Janssen, M., Paillou, P., Lorenz, R., & Wall, S. 2010, Icar, 207, 948
Leopold, L. B., & Maddock, T. 1953, USGSP, 252, 57
Lopes, R. M. C., Malaska, M. J., Schoenfeld, A. M., et al. 2020, NatAs, 4, 228
Lopes, R. M. C., Stofan, E. R., Peckyno, R., et al. 2010, Icar, 205, 540
Lopes, R. M. C., Wall, S. D., Elachi, C., et al. 2019, SSRv, 215, 33
Lora, J. M., Lunine, J. I., & Russell, J. L. 2015, Icar, 250, 516
Lorenz, R., Lopes, R., Paganelli, F., et al. 2008, P&SS, 56, 1132
Lorenz, R. D. 2014, GeoRL, 41, 5764
Lorenz, R. D., Turtle, E. P., Barnes, J. W., et al. 2018, JHATD, 34, 374, https://dragonfly.jhuapl.edu/News-and-Resources/docs/34_03-Lorenz.pdf
Lucas, A., Aharonson, O., Deledalle, C., et al. 2014, JGRE, 119, 2149
Lunine, J., & Atreya, S. 2008, NatGe, 1, 159
Malaska, M., Radebaugh, J., Le Gall, A., et al. 2011, LPSC, 42, 1562
Malaska, M. J., Radebaugh, J., Lopes, R. M. C., et al. 2020, Icar, 344, 113764
Mitchell, K. L., Barmatz, M. B., Jamieson, C. S., Lorenz, R. D., & Lunine, J. I. 2015, GeoRL, 42, 1340
Montgomery, D. R., & Dietrich, W. E. 1989, WRR, 25, 1907
Montgomery, D. R., & Gran, K. 2001, WRR, 37, 1841
Moore, J. M., Howard, A. D., & Morgan, A. M. 2014, JGRE, 119, 2060
Moore, J. M., & Pappalardo, R. T. 2011, Icar, 212, 790
Mull, C. G., Houseknecht, D. W., & Bird, K. 2003, J. Northern Alaska. USGSPR, 1673
Neish, C. D., Molaro, J. L., Lora, J. M., et al. 2016, Icar, 270, 114
Nunn, J. A., Czerniak, M., & Pilger, R. H., Jr. 1987, Tecto, 6, 603
Occhietti, S., Parent, M., Lajeunesse, P., Robert, F., & Govare, É. 2011, Developments in Quaternary Science, 15, 601
Parker, G., Wilcock, P. R., Paola, C., Dietrich, W. E., & Pitlick, J. 2007, JGRF, 112, F04005
Parvis, M. 1950, Highway Research Board Bulletin, 28, 36, http://onlinepubs.trb.org/Onlinepubs/hrbbulletin/28/28.pdf
Perron, J. T., Lamb, M. P., Koven, C. D., et al. 2006, JGRE, 111, E11001
Poggiali, V., Mastrogiuseppe, M., Hayes, A. G., et al. 2016, GeoRL, 43, 7887
Radebaugh, J., Lorenz, R. D., Wall, S. D., et al. 2011, Icar, 211, 672
Radebaugh, J., Ventra, D., Lorenz, R. D., et al. 2018, GSLSP, 440, 281
Seybold, H., Rothman, D. H., & Kirchner, J. W. 2017, GeoRL, 44, 2272
Soderblom, L. A., Tomasko, M. G., Archinal, B. A., et al. 2007, P&SS, 55, 2015
Stofan, E. R., Elachi, C., Lunine, J. I., et al. 2007, Natur, 445, 61
Sudmeyer, R. 2016, Climate in the Pilbara. Government of Western Australia, Department of Primary Industries and Regional Development, 220, https://researchlibrary.agric.wa.gov.au/bulletins/220/
Tewelde, Y., Perron, J., Ford, P. G., Black, B. A., & Miller, S. R. 2013, JGRE, 118, 2198
Tomasko, M., Archinal, B., Becker, T., Bézard, B., et al. 2005, Natur, 438, 765
Torres, R., Snoeij, P., Geudtner, D., et al. 2012, RSEnv, 120, 9
Turtle, E., Perry, J., Barbara, J. M., et al. 2018, GeoRL, 45, 5320
Turtle, E., Perry, J., Hayes, A., & McEwen, A. 2011, Icar, 212, 957
Van Kranendonk, M., Hickman, A., Smithies, R., Nelson, D., & Pike, G. 2002, Economic Geology, 97, 695
Walker, D. A., Walker, M. D., & Everett, K. R. 1985, AAAR, 17, 321
Wall, S., Hayes, A., Bristow, C., et al. 2010, GeoRL, 37, 5202
Wall, S. D., Kirk, R. L., Stiles, B. W., et al. 2019, Cassini RADAR Users Guide. In: JPL Internal Doc.
Wardle, R. J., & Van Kranendonk, M. J. 1996, in Precambrian Crustal Evolution in the North Atlantic Region, Geol. Soc. Publ., Vol. 112, ed. T. S. Brewer, 137
Yamazaki, D., O'Loughlin, F., Trigg, M. A., et al. 2014, WRR, 50, 3467
Yi, R. S., Arredondo, Á., Stansifer, E., Seybold, H., & Rothman, D. H. 2018, Physical and Engineering Sciences, 474